Available online at www.sciencedirect.com
ScienceDirect
Geochimica et Cosmochimica Acta 73 (2009) 729–749
Geochimica et Cosmochimica Acta
www.elsevier.com/locate/gca

Chemical and isotopic fractionation of wet andesite in a temperature gradient: Experiments and models suggesting a new mechanism of magma differentiation

F. Huang [a], C.C. Lundstrom [a,*], J. Glessner [a], A. Ianno [a], A. Boudreau [b], J. Li [a], E.C. Ferré [c], S. Marshak [a], J. DeFrates [a]

[a] Department of Geology, University of Illinois at Urbana-Champaign, 245 NHB, 1301 W. Green St., IL 61801, USA
[b] Nicholas School of the Environment and Earth Sciences, Box 90227, Duke University, Durham, NC 27708, USA
[c] Department of Geology, Southern Illinois University, Carbondale, IL 62901-4324, USA

Received 6 August 2008; accepted in revised form 4 November 2008; available online 18 November 2008

Abstract

Piston–cylinder experiments were conducted to investigate the behavior of partially molten wet andesite held within an imposed temperature gradient at 0.5 GPa. In one experiment, homogenous andesite powder (USGS rock standard AGV-1) with 4 wt.% H_2O was sealed in a double capsule assembly for 66 days. The temperature at one end of this charge was held at 950 °C, and the temperature at the other end was kept at 350 °C. During the experiment, thermal migration (i.e., diffusion in a thermal gradient) took place, and the andesite underwent compositional and mineralogical differentiation. The run product can be broadly divided into three portions: (1) the top third, at the hot end, contained 100% melt; (2) the middle-third contained crystalline phases plus progressively less melt; and (3) the bottom third, at the cold end, consisted of a fine-grained, almost entirely crystalline solid of granitic composition. Bulk major- and trace-element compositions change down temperature gradient, reflecting the systematic change in modal mineralogy. These changes mimic differentiation trends produced by fractional crystallization. The change in composition throughout the run product indicates that a fully connected hydrous silicate melt existed throughout the charge, even in the crystalline, cold bottom region. Electron Backscatter Diffraction analysis of the run product indicates that no preferred crystallographic orientation of minerals developed in the run product. However, a significant anisotropy of magnetic susceptibility was observed, suggesting that new crystals of magnetite were elongated in the direction of the thermal gradient. Further, petrographic observation reveals alignment of hornblende parallel to the thermal gradient. Finally, the upper half of the run product shows large systematic variations in Fe–Mg isotopic composition reflecting thermal diffusion, with the hot end systematically enriched in light isotopes. The overall $\delta^{56}Fe_{IRMM\text{-}14}$ and $\delta^{26}Mg_{DSM\text{-}3}$ offsets are 2.8‰ and 9.9‰, respectively, much greater than the range of Fe–Mg isotope variation in high-temperature terrestrial samples.

In contrast, no obvious chemical differentiation was observed in a similar experiment (of 33 days duration) where the temperature ranged from 550 to 350 °C, indicating the critical role of the melt in causing the differentiation observed in the 950–350 °C experiment. If temperature gradients can be sustained for the multi-million-year time scales implied by geochronology in some plutonic systems, thermal migration could play a heretofore unrecognized role in the development of differentiated plutons. Elemental distributions, dominated by phase equilibria, cannot be used to discriminate thermal migration from conventional magma differentiation processes such as fractional crystallization. However, the observation of Fe–Mg isotopic variations in partially molten portions of the experiment indicates that these isotopic systems could provide a unique fingerprint to this process. This result could also provide a possible explanation for the Fe–Mg isotope variations observed in high-temperature silicate rocks and minerals.

* Corresponding author.
E-mail address: lundstro@uiuc.edu (C.C. Lundstrom).

0016-7037/$ - see front matter © 2008 Elsevier Ltd. All rights reserved.
doi:10.1016/j.gca.2008.11.012

1. INTRODUCTION

The chemical diversity of Earth's igneous rocks is generally thought to reflect the consequences of partial melting and fractional crystallization, with assimilation and magma mixing playing a secondary role. Although temperature gradients must exist in cooling and differentiating magma bodies as well as their surroundings, the role of temperature gradients in magma differentiation has generally been viewed as unimportant because conductive dissipation of heat occurs faster than mass diffusion (Bowen, 1915; Lesher and Walker, 1988). However, recent geochronological observations from plutonic rocks indicate that the cooling time scale of granitic plutons could be long (up to 10 million years) and the processes forming large intrusions must involve more than simple magma injection followed by cooling (e.g., Coleman et al., 2004).

Previous work has documented that significant compositional changes can occur during temperature gradient driven diffusion through silicate materials (Walker et al., 1981, 1988; Walker and DeLong, 1982; Lesher and Walker, 1986, 1988, 1991). If the process occurs solely in a single phase (melt), it is termed Soret diffusion (Walker et al., 1981; Walker and DeLong, 1982; Lesher and Walker, 1986), whereas when it occurs within a partially molten material it is called thermal migration (Buchwald et al., 1985; Lesher and Walker, 1988; Walker et al., 1988). Both thermal migration and Soret processes involve both chemical diffusion (driven by a chemical activity gradient, $d\mu/dx$) and thermal diffusion (driven by a temperature gradient, dT/dx). But the existence of solid phases in thermal migration experiments buffers the chemical activity of components in the melt phase, a phenomenon that doesn't happen during Soret diffusion. Thus, the two processes yield dramatically different compositional trends.

Here, we report results of thermal migration experiments to examine the behavior of wet, partially molten andesite. These experiments, which differ from those of previous studies that did not include water, show the important role of water during thermal migration. Our results indicate that thermal migration in wet silicates can produce significant chemical differentiation of Earth's magmas. Importantly, our results predict that positive co-variations in non-traditional isotope ratios (Mg or Fe isotopes) develop during thermal migration and provide a unique fingerprint to this process. Thus, study of non-traditional isotope ratios serve as a means to test whether thermal migration in wet magma occurs in nature.

2. THERMAL MIGRATION EXPERIMENTS

The goal of the experiments described here was to examine the thermal migration process operating in a wet andesite. All experiments used USGS standard AGV-1 (200 mesh) (Flanauan, 1967), a rock powder of andesitic bulk composition with nanopure water added prior to the experiment and sealed in noble metal capsules. The experiments were run in a 3/4″ piston cylinder apparatus (Rockland Research) at 0.5 GPa using NaCl-pyrex assemblies with a 10% friction correction applied. The hot-spot temperature was controlled using an S-type thermocouple.

Multiple experiments having double thermocouple arrangements run at the same output power conditions provide a well-constrained temperature profile for these experiments (Fig. 1). Two separate experiments with durations of 24 h at identical output power conditions measured the temperature at the base of the experimental assembly (the bottom of the capsules in experiments #1 and #2) to be 352 ± 5 °C. Another experiment measured the temperature at the top of the assembly (base of the base plug) to be

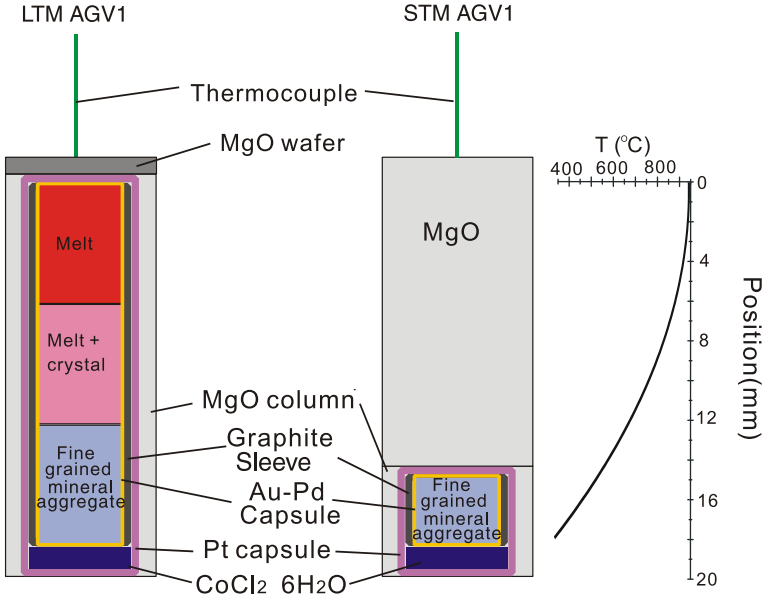

Fig. 1. Schematic diagram of the set up of the two experiments. On right is shown the temperature profile for this assembly. Temperature profile for these experiments was obtained by multiple experiments using double thermocouple arrangements run at the same output power conditions.

481 °C. Combining these data with the hot-spot temperature of 950 °C, we used a second order polynomial fit (e.g., Pickering et al., 1998) to estimate the temperature profile in these experiments. This low temperature agrees with temperatures measured at the bottom of a similar ¾″ NaCl-pyrex assembly by (Watson and Wark, 1997).

2.1. Experiment #1—long thermal migration AGV-1 (LTM-AGV-1)

This experiment utilized a ~2 cm-long sealed double capsule placed in a temperature gradient which ranged from 950 °C down to ~350 °C (Fig. 1). The experiment duration was 66 days. At the start of the experiment, AGV-1 powder plus 4 wt.% water were loaded into a 3 mm diameter $Au_{75}Pd_{25}$ capsule which was arc welded. The capsule was placed inside a 5 mm (OD) thick-walled Pt capsule, with a thin graphite liner placed between the two capsules. 20 mg of $CoCl_2.6H_2O$ was placed at the bottom of the Pt capsule to provide water in the outer capsule. The oxidized form of Co should also act to keep the inner capsule oxidizing by reacting with H_2, if present. The Pt capsule was welded and placed in the piston cylinder surrounded by crushable MgO. The top of the capsule was positioned in the center of the hot-spot and the bottom of the capsule located only 2 mm above the top of the piston with 1 mm-thick MgO and graphite wafers separating the capsule from the piston.

The charge was initially taken to 0.5 GPa pressure and the hot-spot temperature was increased at 100 °C/min to 950 °C. After 1 day, the experiment was switched from direct temperature control to constant output power, and remained this way for the next 65 days. The thermocouple continued to read 950 °C for several weeks before deviations indicated contamination. However, we observed no significant changes in either amperes or voltage during the course of the experiment, indicating that the hot-spot temperature remained constant at 950 °C (±10 °C) for the full duration. Although $f(O_2)$ of the experiment was unbuffered, the lack of H_2O or Fe loss implies that conditions in the experiment were oxidizing (>QFM), consistent with previous experiments in which H_2O was added directly (Kushiro, 1990). Turning off the power resulted in a rapid quench, with hot-spot temperature dropping hundreds of degrees within a few seconds. Most of the discussion and data in this paper reflect observations made on the run product of this 66 day long LTM AGV-1 experiment.

2.2. Experiment #2—short thermal migration (STM AGV-1)

For this experiment, we positioned a ~3 mm long gold capsule with 4 wt.% water (sealed by welding) at the bottom of thick-walled Pt double capsule. With the same output power and geometry as the LTM AGV-1 experiment, the temperature ranged from ~350 °C at the bottom of the capsule to ~550 °C at the top (Fig. 1). This experiment ran for 33 days. Its purpose was to compare the thermal migration process occurring in the absence of melt to that in an experiment in the presence of melt, LTM-AGV-1.

3. ANALYTICAL METHODS

The run products of our experiments were sectioned longitudinally with one half of the run product mounted in epoxy for microanalysis and the other half used for isotopic analysis. Bulk compositions as a function of position in the run products were determined by the average of two standards-based energy dispersive (EDS) X-ray analyses using a 250 μm^2 raster on the JEOL 840A scanning electronic

Table 1
Modes (%) of melt and minerals in experiment LTM-AGV-1.

Position (mm)	Melt	Apatite	Fe–Tioxide	Amphibole	Plagioclase	Biotite	K-spar	Quartz
16	100							
16	100							
14.7	100							
13.5	100							
12.6	97	3						
12.6	97	3						
10.9	82		14	4.4				
10.9	78		17	5.4				
10.4	52		2.9	45				
9.4	37		2.1	42	18			
9	15	1	0.5		84			
8.4	22	2	1.0	17	57			
8.4	21	1	4.1	19	55			
7.5	2.8		3.7	14	80			
6.5			3.0	1.4	85	10		
5			1.1		78	20		
5			1.3		86	13		
4.3			2.1		76	17	5	
3.4			1.3		71	12		15
2.2			0.3		59	9.2		31
1.5			0.6		43	9	24	24
0.5			1.0		29	6	25	39
0					40	7	23	29

microscope in the Department of Geology, University of Illinois at Urbana-Champaign (Table 1). The acceleration voltage during analysis was 15 kV and the beam current was 30 nA. EDS analyses used a 4Pi revolution software system with full ZAF corrections performed. Smithsonian standards Kakanui hornblende and Arenal hornblende were used as primary and secondary standards for amphibole analysis (Table 2). Major element compositions for amphiboles were corrected based on the slight difference between measured and true values of the Arenal hornblende standard. To evaluate Mg–Fe exchange for amphibole-melt, we had to assume that Na volatilization during measurement of small spots of hydrous melt (which undoubtedly occurred) resulted in no change in Mg/Fe ratio, allowing determination of $^{\text{melt-amph}}K_{\text{Fe–Mg}}$. Plagioclase compositions were measured using anorthite glass (for Ca, Al, Si) and VG-2 (for Na, Fe, and K) for calibration with Lake County plagioclase measured as a secondary standard (Table 3). Modes of minerals and melt were measured by digital image processing of multiple BSE 250 × 250 μm images as a function of position in combination with X-ray maps of a variety of elements.

We measured bulk water contents by raster analysis (500 × 500 μm) using a Cameca 5f SIMS in the Center for Microanalysis of Materials of the University of Illinois at Urbana-Champaign using standard energy filtering techniques with O^- beam (Pertermann and Lundstrom, 2006) and silicate glass standards for the calibration (kindly provided by E. Hauri). Analyses of F and Cl used the 5f with 10 nA Cs+ beam, following methods in Hauri et al. (2002). Trace-elements were analyzed using a 250 × 250 μm raster analysis, energy filtering of 75 V offset, and a primary beam of 12.5 kev O^- ions and 17–19 nA current. Repeated analyses of the NIST 610 glass show precision for most trace-elements of 10% (1s). We used a 50 V offset voltage during SIMS analyses (with same beam conditions) of selected trace-elements in plagioclase and coexisting glass to determine partitioning. For these analyses, a field aperture setting of 3 was selected to spatially resolve analyses after imaging the locations of crystal and melt. Although no calibration standards were used for these measurements, the analyses provide quantitative partition coefficients as long as the useful yields of both phases is similar, as is typically assumed in partition coefficient determinations using SIMS.

We measured Fe and Mg isotope compositions in mg sized chips taken from the half of LTM-AGV-1 that was not turned into a surface mount. Analyses used a Nu Plasma HR MC-ICP-MS located in the Department of Geology, University of Illinois at Urbana-Champaign (Table 4). The chips, along with several USGS rock standard powders including AGV-1 and BCR-2, were digested in a mixture of concentrated HF and HNO_3. Fe and Mg were then separated by anion and cation resin chromatography, respectively. Fe isotope analyses were measured in pseudo-high resolution mode by both sample-standard bracketing and double-spike methods and agree within error with repeat analyses indicating a 2 s precision of 0.1‰. Mg isotopic compositions on each chip were measured multiple times using an in-house standard for bracketing and multiple DSM-3 analyses to determine absolute scale. These were interspersed throughout the session and indicate a 2 s precision of 0.2‰ on δ^{26}Mg.

Anisotropy of Magnetic Susceptibility (AMS) was measured using a Kappabridge KLY-4S AC induction bridge located at Southern Illinois University under a field of 300 A/m. The 1" epoxy round mount with the brass sample ring removed was placed directly into the homogenous field and measured in manual mode. Directional accuracy is estimated to be better than 2°. A magnetic hysteresis experiment using a Vibrating Sample Magnetometer Princeton 3900-4 under fields up to 1591 kA/m was performed on the same specimen.

Electron Backscatter Diffraction (EBSD) measurements were made on the JEOL 7000F Analytical SEM located in the Center for Microanalysis of Materials located at UIUC. An HKL Technology EBSD System with high resolution camera was used for crystallographic measurements and phase identification with forward scatter detector for crystallographic contrast imaging. A more detailed description of the EBSD procedure will be presented elsewhere.

We used the model IRIDIUM (Boudreau, 2003) to simulate the diffusion-reaction processes in LTM-AGV-1. IRIDIUM couples a mineral-melt thermodynamic minimization routine with transport equations (diffusion, advec-

Table 2
Major element compositions (wt.%) of amphiboles in LTM-AGV-1.

Position (mm)	11 ($N = 6$)	10.5 ($N = 3$)	9.5 ($n = 2$)	8.8 ($n = 3$)	8.5 ($n = 5$)	7.8 ($n = 1$)	Arenal hornblende	
							Measured	True
SiO_2	40.73(25)	40.20(53)	41.12(58)	42.43(1.34)	41.29(16)	44.58	42.31	41.46
TiO_2	2.42(14)	2.07(22)	2.51(8)	2.01(13)	2.04(20)	1.59	1.45	1.41
Al_2O_3	14.35(19)	14.66(10)	13.30(1.49)	12.58(1.30)	12.85(51)	9.80	15.36	15.47
FeO	15.28(57)	15.15(21)	17.03(33)	16.06(1.01)	20.39(1.36)	17.94	11.66	11.47
MgO	11.45(49)	11.64(24)	9.68(12)	11.06(54)	8.65(78)	9.99	15.43	14.24
CaO	12.50(29)	13.06(79)	13.06(1.19)	12.79(95)	11.62(20)	13.25	11.57	11.55
Na_2O	2.09(5)	2.02(5)	2.03(26)	1.97(20)	2.08(6)	1.94	2.03	1.91
K_2O	1.17(8)	1.21(7)	1.26(16)	1.10(18)	1.09(5)	0.90	0.18	0.21
Total	100	100	100	100	100	100	100	97.72
Mg#	57.2	57.8	50.3	55.1	43.0	49.8	70.2	68.9

N stands for the number of analyses. 40.73(25) and 42.43(1.34) read as 40.73 ± 0.25 and 42.43 ± 1.34, respectively. The errors in parentheses are 1s of a few analyses. SEM analyses normalized to 100% totals. H_2O content is not accounted in amphiboles.

Table 3
Major element compositions (wt.%) and mineral component of plagioclase at the plagioclase-rich layer in LTM-AGV-1.

Sample	plag11rim	plag11core	plag10	plag13	plag15	plag18	plag21	Lake County plg	
								Measured	True
SiO_2	58.84	56.33	54.27	56.35	55.49	54.62	54.09	50.69	51.25
Al_2O_3	26.58	28.07	29.33	27.5	27.87	28.95	29.08	31.93	30.91
FeO	0.14	0.06	0.35	0.77	0.92	0.53	0.57	0.19	0.46
CaO	7.83	9.39	10.46	8.93	9.72	10.41	10.77	13.24	13.64
Na_2O	5.5	5.82	5.18	5.91	5.45	5	4.89	3.81	3.45
K_2O	1.11	0.33	0.4	0.54	0.56	0.49	0.6	0.14	0.18
Total	100	100	100	100	100	100	100		
Cations in plagioclase in an 8 oxygen basis									
Si^{4+}	2.63	2.53	2.45	2.54	2.51	2.47	2.45		
Al^{3+}	1.40	1.49	1.56	1.46	1.48	1.54	1.55		
Fe^{2+}	0.01	0.00	0.01	0.03	0.04	0.02	0.02		
Ca^{2+}	0.37	0.45	0.51	0.43	0.47	0.50	0.52		
Na^{+}	0.48	0.51	0.45	0.52	0.48	0.44	0.43		
K^{+}	0.06	0.02	0.02	0.03	0.03	0.03	0.04		
Total	4.94	4.99	5.01	5.01	5.01	5.00	5.01		
Component in plagioclase									
Al (%)	52.1	51.8	46.2	52.8	48.7	45.1	43.5		
An (%)	41.0	46.2	51.5	44.1	48.0	51.9	53.0		
Or (%)	6.9	1.9	2.3	3.2	3.3	2.9	3.5		

Al, An, and Or stand for albite, anorthite, and orthoclase, respectively. All data but plag11rim reflect core (center of grain) analyses.

Table 4
Variation of bulk major element compositions and H_2O (wt.%) along experiment LTM-AGV-1.

Position (mm)	0	1.8	3	4.5	6	7.5	9	10.8	11.8	12.8	14.5	16.5	18
SiO_2	72.29	69.19	66.11	55.10	57.15	55.44	52.29	54.01	54.64	59.43	62.34	61.96	62.02
TiO_2	0.50	0.63	0.65	0.83	0.67	0.87	1.23	1.15	1.60	0.81	0.89	0.96	0.90
Al_2O_3	12.79	14.07	16.01	20.93	21.47	21.06	18.05	15.82	16.11	17.26	17.81	18.18	18.32
FeO	3.05	4.25	3.91	5.71	4.82	5.78	8.13	8.53	12.22	3.36	3.72	3.42	3.56
MgO	1.33	1.60	1.51	2.02	1.78	2.28	3.57	4.54	1.63	1.75	1.79	1.79	1.56
CaO	2.14	3.75	4.11	5.72	5.61	6.83	10.39	8.02	4.93	6.60	5.04	5.01	5.11
Na_2O	1.80	2.86	3.71	5.35	5.89	4.63	3.51	3.59	3.91	4.19	4.08	4.17	4.23
K_2O	5.13	2.68	3.03	2.63	1.76	2.00	1.50	2.61	2.89	3.15	3.36	3.49	3.54
P_2O_5	0.99	0.99	0.99	1.73	0.87	1.13	1.34	1.73	2.08	3.48	0.99	1.04	0.79
Mg#	43.8	40.2	40.8	38.7	39.8	41.3	44.0	48.7	19.2	48.2	46.2	48.3	43.9

Position (mm)	0	3.4	6.5	9.4	12.6	13.5	16
H_2O (wt.%)	0.62	0.83	2.88	4.51	7.02	7.6	7.47

tive infiltration and compaction). We used an 11-node distribution over 2 cm with temperature linearly varying from 950 to 680 °C and only allowed diffusive transport (program set to infiltration mode with the infiltration rate set to 0). Orthopyroxene saturation was suppressed. Initially, each node had the same AGV-1 bulk composition with 4 wt.% H_2O added and normalized to 100%. The pressure was set to 0.5 GPa. Diffusivities were set at 1×10^{-7} cm^2/s for all oxides except Na_2O and K_2O, which were set at 1×10^{-6} and H_2O, which was set at 1×10^{-4}. The 10^{-7} diffusivities are similar to those expected for a wet silicate melt near 1000 °C (Brady, 1995); the higher diffusivities of alkalis and water are estimated based on the relatively greater diffusivities for these components in silicate melts. Soret coefficients were those given in Lesher and Walker (1991) for Mount Hood Andesite.

4. RESULTS

4.1. Experiment LTM-AGV-1

4.1.1. Phase distribution and composition

The LTM-AGV-1 run product varies in color from dark at the hot end to light at the cold end (Fig. 2), reflecting the progressive change in phase assemblage and composition as a function of spatial position. The upper third of the run product—the end at highest temperature—consists of glass (quenched melt) only. The middle-third consists of glass coexisting with minerals with mineral proportions increasing with decreasing temperature. The bottom third consists of a fine-grained aggregate of minerals with only minor porosity (<3%). The exact porosity is unknown because it is difficult to distinguish residual pores from pores created

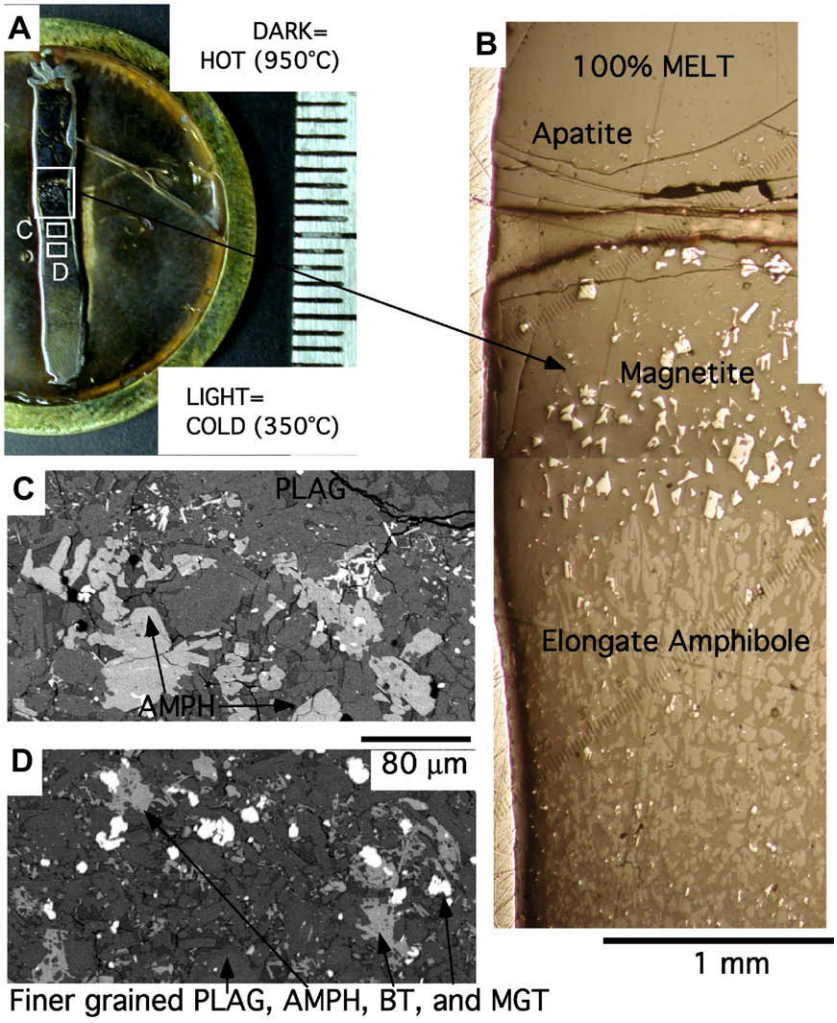

Fig. 2. (A) Reflected light photo of LTM-AGV-1; note the lighter color of the material on the cold end and darker color on the hot end (mm scale at right). (B) Reflected light photomicrograph of the top portion of experiment; the sequence of crystallization is observed to be apatite, then magnetite, and then amphibole. Note the elongation of amphibole crystals toward the top end of the amphibole-saturated area. (C) Backscattered electron (BSE) image of the area just above the texture interface at 8 mm. White phase: FeTi oxides; light gray: amphibole; thin light gray crystals: biotite; dark gray: plagioclase; darkest gray: glass/melt. Note the large amphiboles with euhedral faces growing up temperature gradient. Above these amphiboles occurs a plagioclase-rich layer (at top). Scale bar shown refers to both C and D. (D) BSE image of area just below interface. Same mineral identification as in C. Note the finer-grained nature of minerals and greater presence of biotite. Mineral acronyms: plag, plagioclase; amph, amphibole; bt, biotite; and mgt, magnetite.

by sample preparation plucking. Although we have not performed an "upside down" experiment with cold end above hot end, previous thermal migration studies (Lesher and Walker, 1988; Walker et al., 1988) demonstrated that such experiments evolve to a crystal-rich portion lying above a melt-rich portion, indicating the increasing crystallinity reflects the direction the temperature gradient and not the direction of the gravitational field.

Mineral textures change as a function of position in the run product, probably indicating important changes in the liquid composition. In the middle-third, where abundant glass exists, crystals are larger (up to 100 μm) and have euhedral to sub-euhedral shapes. At a position 8.5 mm above the capsule base (henceforth, all distances referenced to in this paper refer to distance above the capsule base), even larger euhedral and sub-euhedral amphiboles grow upward into glass whereas below it, an aggregate of finer-grained minerals (up to 150 μm) with only minor (<3%) interstitial material exists (Fig. 2C and D). A ~1 mm-thick layer almost entirely composed of plagioclase lies just above the zone that contains large amphiboles.

Minerals appear sequentially from top to bottom of the run product. The order of appearance—apatite, titanomagnetite, ilmenite, amphibole, plagioclase, biotite, quartz, and K-feldspar (clinopyroxene, titanite, fluorite, and zircon also occur as minor phases)—is consistent with saturation temperatures expected (Fig. 3). Phase modes smoothly vary as a function of temperature along the run product (Table 1), and modes of discernible melt vary from 100% at the top (hot) end to 0% at ~6.5 mm. Euhedral and sub-euhedral apatites are the first to appear at ~12.8 mm and continue throughout the charge (Fig. 4-Spot 5). Abundant titano-

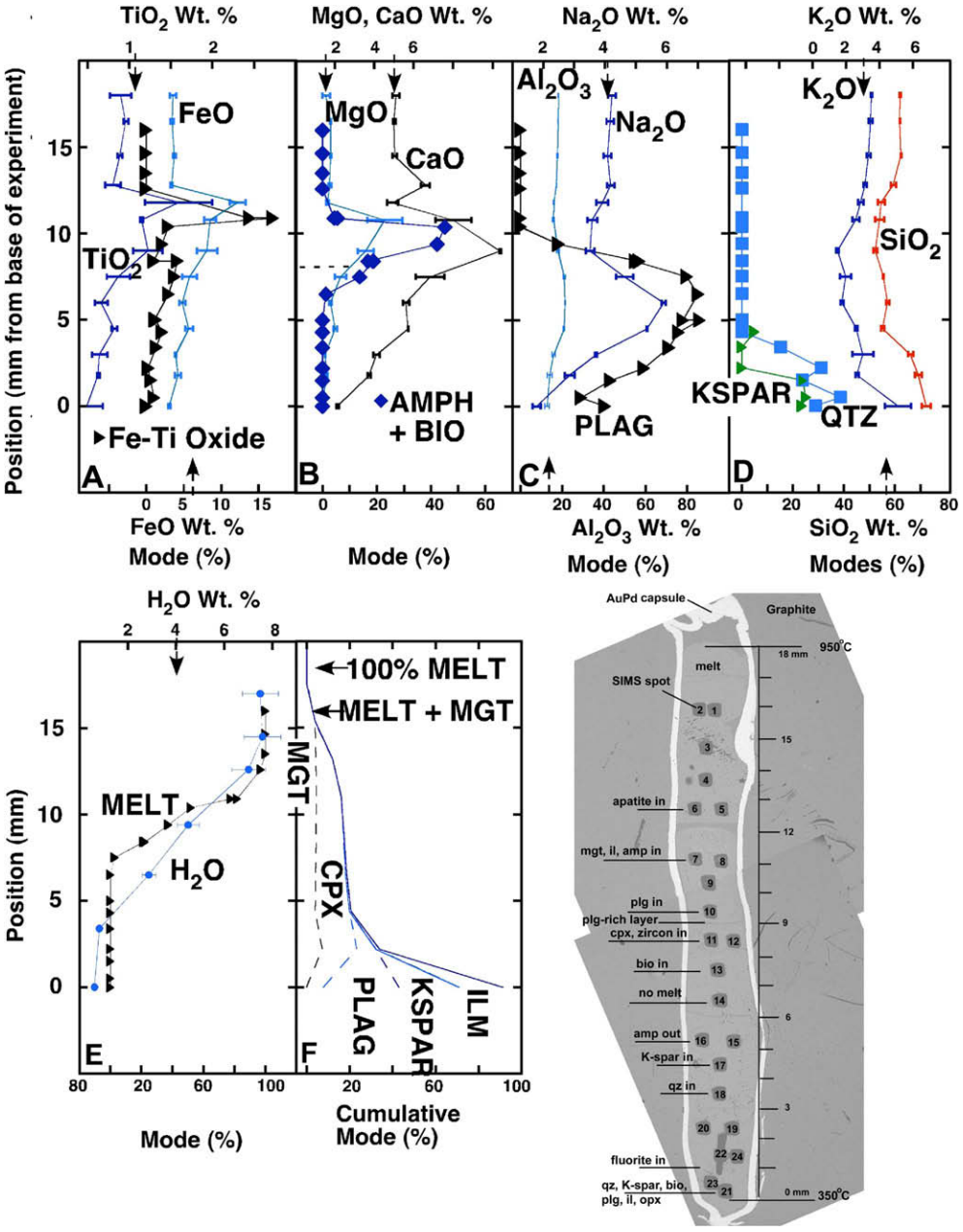

Fig. 3. BSE image, major element compositions, and mineral and melt modes of LTM-AGV-1 and IRIDIUM simulation. At bottom right is a BSE image of the experiment with the SIMS raster analysis locations shown (# given). Approximate locations of mineral arrival given; mgt, magnetite; il, ilmenite; amp, amphibole; cpx, clinopyroxene; bio, biotite; K-spar, K-feldspar; qz, quartz. A–E) Variation of mineral modes and bulk composition oxides as a function of distance from the base (cold end) of experiment. The compositional variation in the fully molten, upper third is small. Note the strong correspondence between peaks in oxide concentration and particular mineral modes and the rapid increase in SiO_2 (up to 73 wt.%), K_2O, quartz and K-spar at the base of the experiment, corresponding to a granitic bulk composition. Dashed vertical arrows showing the initial oxide compositions in AGV-1 (indicative of mass balance) while the dashed horizontal line in B shows approximate transition between amphibole and biotite. The overall trends in composition indicate that the andesite has chemically differentiated by thermal migration to a more mafic hot end and a granitic composition cold end. Error bars shown are 1 SD. F). Cumulative mineral modes predicted by IRIDIUM (top to bottom from 950 to 700 °C) after a 50 day diffusion-reaction simulation (see text and methods for details). Note enrichment in melt mode at top and K-spar and plagioclase modes at base.

magnetite and minor ilmenite occur from 12 mm down, followed by elongate amphiboles occurring from ~11.2 mm down to 6.5 mm (Fig. 4-Spot 7). At 6.5 mm, biotite replaces amphibole as the dominant mafic mineral.

Plagioclase appears at 9.5 mm, reaches a maximum mode (84%) at 9 mm and decreases down to the bottom of the run product. Abundant quartz and potassium feldspar (K-spar) occur near the capsule bottom. K-spar

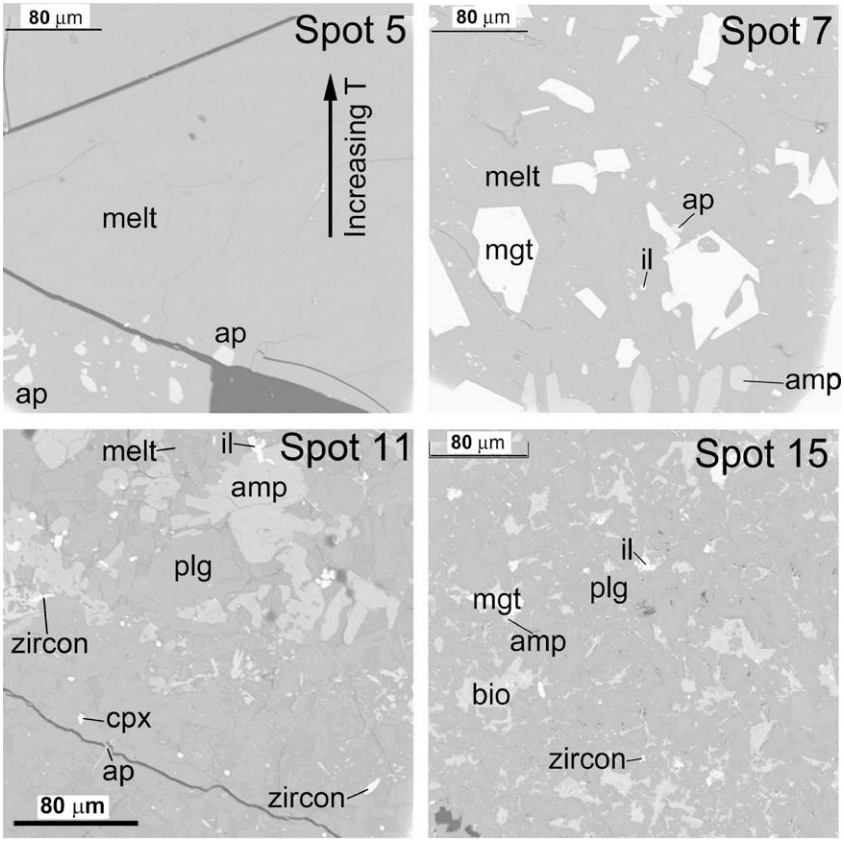

Fig. 4. BSE images for SIMS analysis spots 5, 7, 11, and 15 (located in Fig. 3). Apatite is the liquidus mineral at Spot 5. Euhedral and sub-euhedral Fe–Ti oxides and elongated amphibole occur at Spot 7. Zircon crystals up to 8 μm occur at Spot 11 and 15.

patches are irregularly shaped and occur as parts of larger, euhedral-shaped feldspar crystals with the remainder of the crystal being plagioclase. Small quartz crystals form a matrix around these larger feldspar grains (Fig. 5 or a color version in Electronic annex S-Fig. 1). Thus, the bottom portion of the run product consists predominantly of plagioclase, K-spar, and quartz—i.e., a granitic mineral assemblage.

Important accessory minerals (e.g., zircon, fluorite, and titanite) also occur in the lower half of the run product.

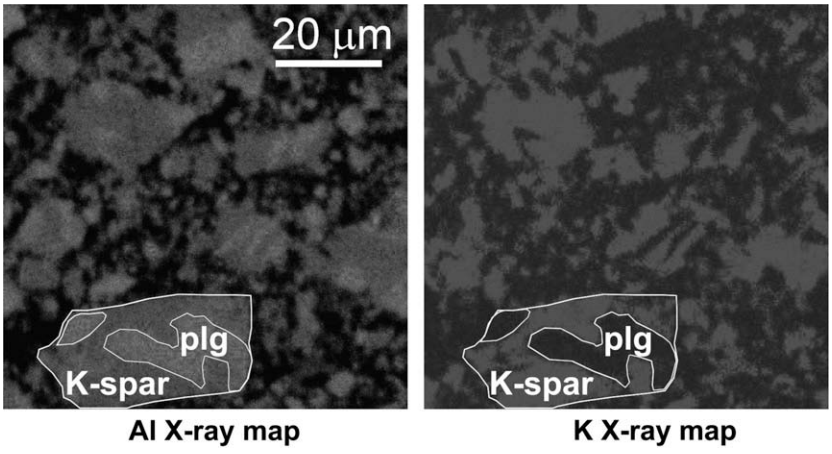

Fig. 5. X-ray maps (1000×) of Al and K for a location 1 mm above the bottom. The Al X-ray map defines a sub-euhedral feldspar crystal, interpreted to possibly reflect an original plagioclase in the starting material. Examination of the K X-ray maps shows that this crystal is actually made up of prominent domains of K-spar and plagioclase, with the interpretation that K-spar has replaced plagioclase.

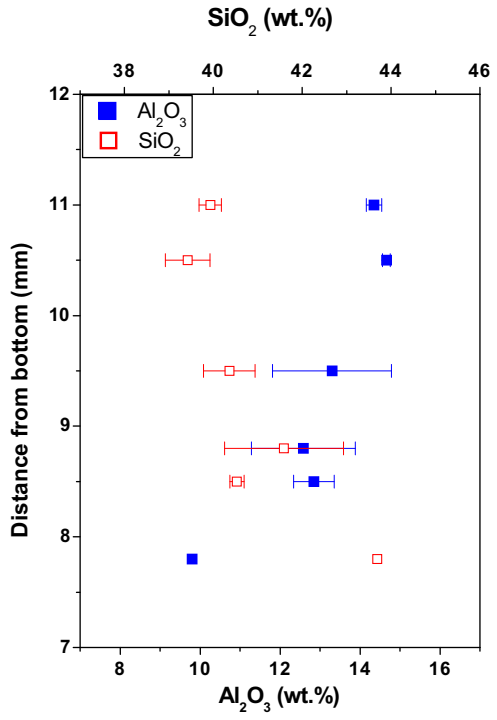

Fig. 6. Al_2O_3 and SiO_2 contents of amphibole as a function of position. Both trends are consistent with expected amphibole composition with decreasing temperature.

Because the known trace-element homogeneity of AGV-1 indicates that the original powder does not contain minerals such as zircon, these minerals likely crystallized during the experiment. Zircon crystals up to 8 μm across occur in the run product at SIMS spots 11 and 15 (Fig. 4), fluorite crystals occur in the bottommost portion of the experiment, and titanite was positively identified at ~6.5 mm.

4.1.2. Major element compositions of phases and bulk

Bulk chemical composition smoothly varies down the temperature gradient, reflecting the clear correspondence between mineral modes and oxide concentrations (Fig. 3). Bulk H_2O content decreases from 7 wt.% at the top to less than 1 wt.% at the bottom, in parallel with decreasing amounts of melt, indicating nearly constant H_2O content in the melt in the upper half of the charge. FeO and TiO_2 contents peak in the area where the most abundant Fe–Ti oxides occur (Fig. 3A). MgO and CaO contents are coincident with variations in the amphibole mode (Fig. 3B), whereas Na_2O and Al_2O_3 contents coincide with the plagioclase mode (Fig. 3C). SiO_2 content is constant within the glass-rich top, decreases in the middle portion due to the presence of Fe–Ti oxides and amphibole, and then increases significantly in the bottom portion as quartz and K-spar mode increase. In summary, the major element composition correlates dramatically with the phase proportions which directly reflect the temperature gradient, resulting in the formation of a granitic bulk composition with 5.1 wt.% K_2O, 12.8 wt.% Al_2O_3 and 1.8 wt.% Na_2O and 72.3 wt.% SiO_2 in the almost fully crystalline bottom portion (Fig. 3D).

Phase compositions also change systematically through the run product. The SiO_2 content and Al_2O_3 of amphibole

Table 5
Trace-element compositions (ppm) in experiment LTM-AGV-1.

Position (mm)	Sample	Li	Cr	Ni	Rb	Sr	Y	Zr	Ba	La	Nd	Sm	Lu	Hf	Th	U	F*
16	#1	260	3.8	56	160	780	19	250	3170	51	38	11	0.4	6.7	8.2	2.8	
16	#2	260	4.4	53	160	740	18	250	3180	49	37	5.7	0.4	8.3	7.7	2.5	
14.7	#3	230	5.7	78	170	790	19	260	3440	52	30	7.6	0.4	8.5	6.3	2.2	170
13.5	#4	260	4.1	43	160	750	20	250	3140	50	32	3.9	0.4	9.1	6.9	2	
12.6	#5	210	4.5	61	160	710	19	230	2980	48	31	6.6	0.4	8.3	5.6	1.6	
12.6	#6	220	3.5	41	130	680	17	230	2870	46	35	6.2	0.2	5.6	7.3	1.6	
10.9	#7	200	8.6	86	130	630	23	220	2580	52	34	8.4	0.4	6.6	6.9	1.6	52
10.9	#8	200	16	160	130	650	24	240	2770	61	55	9.2	0.7	7.5	6.9	2.8	
10.4	#9	140	23	170	91	580	43	230	2030	50	65	15	0.9	8.6	5.3	2.3	
9.4	#10	140	41	170	96	600	32	220	1520	47	56	12	0.5	7.4	5.4	1.1	46
8.4	#11	67	19	110	54	1300	55	550	1250	154	140	35	0.8	13.7	22	2.3	
8.4	#12	100	15	95	68	990	19	300	1220	46	40	8.5	0.4	6.4	5	2	
7.5	#13	80	25	120	140	870	26	390	2300	55	41	14	0.4	6.2	7.7	3.1	
6.5	#14	67	18	90	170	800	26	380	2040	40	37	9.9	1.1	7.7	10	3.6	
5	#15	26	13	250	200	630	30	530	2300	153	110	15	1.2	18.4	20	6.1	74
5	#16	23	11	150	130	680	9.2	10	1990	45	42	7.4	0.2	0.7	3.1	0.7	
4.3	#17	25	31	290	240	730	23	170	2550	54	43	11	0.4	7.1	4.8	2.8	
3.4	#18	19	19	160	150	780	24	500	2270	39	35	8.4	0.3	11.6	11	6.3	
2.2	#19	19	8.7	130	150	400	11	170	860	28	18	4.5	0.3	3.2	5.8	2.3	19
2.2	#20	12	20	110	82	370	13	240	630	22	25	5	0.4	5.4	3.5	2.6	
1.5	#22	20	3.2	43	160	470	13	230	2060	24	20	4.3	0.3	6	5.4	2.5	
1.5	#24	12	3.1	52	210	480	11	170	1210	25	23	4.1	0.3	4.2	4.3	2	
0.4	#23	15	2.3	53	240	380	9.6	130	1410	21	19	4	0.2	3.6	3.4	0.9	
0	#21	12	6.5	67	260	440	8.3	110	1770	25	18	4.1	0.4	3.2	4.1	1.8	174

* Analyzed in separate session using Cs^+ beam.

increase and decrease, respectively, down temperature (Table 2; Fig. 6). The anorthite (An) contents of plagioclase cores decrease down temperature until position 7.5 mm, where they then begin to increase again. Plagioclase throughout the experiment shows a notable texture of thin, abruptly lower An content rims surrounding higher An cores; in the plagioclase-rich layer, cores have 46% An while rims 41% (Table 3, Electronic annex S-Fig. 2). While analyses of the small K-spar domains at the bottom are difficult, two analyses indicate a K_2O/Na_2O of 14.6, equivalent to Or_{90} composition.

While analyses of the lower third indicate a bulk water content of ~0.5 wt%, it is not clear whether this water was present during the experiment or was introduced after it during sample preparation. Nevertheless, the final elemental distribution in the run product clearly requires a medium for fast transport, so we thus infer that H_2O-rich melt was present throughout the lower third of the experiment (see discussion). No bubbles were observed anywhere in the run product, consistent with H_2O being under-saturated in the silicate melt in the upper half of the experiment.

4.1.3. Trace-elements

Trace-elements also vary as a function of position reflecting the phases present and the relative partitioning between phases (Table 5). For instance, Li is highly incompatible in most minerals present, so its concentration systematically follows the melt mode (Fig. 7a). Similarly, Rb concentration is high in the glassy top portion, decreases with decreasing melt mode but then increases again near the bottom where the K-spar mode increases (Fig. 7b). The Sr concentration dramatically increases at 9 mm, coinciding with the peak in plagioclase mode but decreases down temperature such that the Rb/Sr varies from < 0.05 to > 0.6 in the charge (Fig. 7b). Spikes in elevated Hf and Zr contents appear to occur randomly, resulting in large concentration differences between two analyses at the same distance from bottom (for instance, compare SIMS spot 11 vs 12; Fig. 7c). Subsequent BSE imaging shows zircons up to 8m long in the analysis area having a Zr-Hf spike but no zircon present in the analysis area with lower Zr-Hf content. Bulk fluorine content is highest in the bottom region, consistent with the observation of fluorite here.

Because the low REE contents lead to poorer counting statistics, REE contents show more variability than Sr or Rb but still display systematic behavior. For instance, the middle of the run product has the highest middle and heavy REE contents (Nd, Sm, Y, and Lu), consistent with the presence of zircon and amphibole in this region. The La content (representative of the LREE) decreases progressively from the top to bottom (Fig. 7d), reflecting the general incompatibility of La in solids (i.e., its greater presence in the melt) and its compatibility in apatite. Finally, Ding et al. (2007) report systematic changes in Nb/Ta with position, varying from 25 down to 7, reflecting the distribution of amphibole and titanite in the experiment.

To further understand the trace-element partitioning occurring between phases during the experiment, we analyzed the relative trace-element compositions of plagioclase and melt in the plagioclase-rich layer (Table 6). These analyses produce a $^{plagioclase/melt}D_{Sr}$ (the partition coefficient for Sr between plagioclase and melt) of 3.2, while Li, K, Rb, and Ba show general incompatibility (Ds of 0.33, 0.37, 0.29, and 0.81, respectively). The partition coefficients of incompatible elements are slightly greater than previous studies on partitioning of these elements between plagioclase and melt (Morse, 1992; Bindeman et al., 1998), possibly due to inclusion of small melt inclusions during the SIMS analysis of plagioclase.

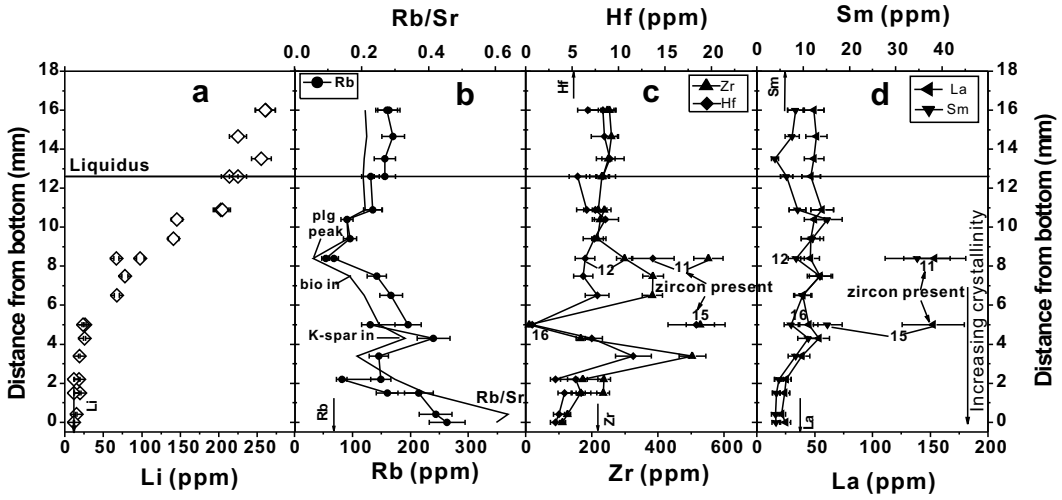

Fig. 7. H_2O and trace-element content and ratio profiles with distance from bottom. Error bars are from 1 SD of 8 analyses of NIST 500 ppm glass. (a) H_2O and Li contents decrease smoothly from the top melt to bottom crystalline portion, consistent with the variation of mode of melt. (b) Rb is enriched in melt and K-bearing minerals. Rb/Sr varies clearly with mode of plagioclase, biotite, and K-feldspar. (c). Zr and Hf contents vary as a function of distance from bottom. Occurrence of zircons in SIMS spots 11 and 15 results in higher Zr and Hf contents than spot 12 and 16, respectively. (d) La and Sm are relatively enriched in melt and amphibole area. Spot 11 and 15 with zircon crystals and large apatite modes have higher REE contents than spot 12 and 16, respectively. H_2O content is from Table 4.

Table 6
Partition coefficients of Li, K, Rb, Sr, and Ba between plagioclase and melt in experiment LTM-AGV-1.

	Li	K	Rb	Sr	Ba
$^{Plg/melt}D$	0.33	0.37	0.29	3.20	0.81
Error (1δ)	0.20	0.20	0.23	0.64	0.15

Although the absolute trace-element concentrations in the melt and plagioclase are not available without standard calibration using NIST glass during the analyses, partition coefficients of Li, K, Rb, Sr, and Ba between plagioclase and melt in the plagioclase-rich layer can still be calculated based on the relative yields to silica of the trace-elements in the two phases assuming similar useful yields between glass and plagioclase.

4.1.4. AMS fabric and EBSD

LTM-AGV-1 displays a magnetic susceptibility ($\approx 30 \times 10^{-6}$ [SI]) about 2 orders of magnitude greater than the practical sensitivity of the instrument (Table 7). This magnetic susceptibility cannot be due to the epoxy resin because the anisotropy (~1.20) is too large to reflect the paramagnetic epoxy. The symmetry of the magnetic susceptibility ellipsoid is prolate (cigar shaped, $T \sim -0.34$) indicating the anisotropy of magnetic susceptibility (AMS) originates from existence of elongate magnetic minerals. The three principal axes of the AMS ellipsoid are oriented sub-parallel to the symmetry axes of the charge with the K_1 axis (the long axis or the magnetic lineation) being nearly parallel to the long axis of the run product (i.e., the thermal gradient). The K_3 axis (the short axis, which is perpendicular to the magnetic foliation plane) is nearly perpendicular to the long axis of the run product. The small deviation in radial symmetry reflects the disk-shaped paramagnetic epoxy. A magnetic hysteresis test indicates that the type of phase responsible for the AMS fabric was multi-domain magnetite, with grain size larger than 10 microns and a saturation field $H_s \approx 40$ kA/m.

EBSD structural refinements on one 300×300 μm area located at height 6.5 mm above the base of the run product show no crystallographic preferred orientation of any mineral. The percentage of successfully indexed minerals is low, reflecting the complexity of the phases and difficulty in polishing the charge to an ultra-flat surface. While EBSD of the middle portion of the charge did not show preferred orientation, the elongate nature of hornblendes in the upper half of the experiment document a clear alignment of the hornblende C axis with the direction of maximum temperature gradient.

4.1.5. Fe and Mg isotope analysis

Non-traditional stable isotopes (e.g., Fe and Mg) are significantly fractionated in the upper half of the run product. $\delta^{56}Fe_{IRMM\text{-}14}$ and $\delta^{26}Mg_{DSM\text{-}3}$ (the per mil deviations in Mg and Fe isotope ratios relative to a standard) vary systematically as a function of position (Table 8 and Fig. 8). While the bottom, crystal-rich portions (PCD and PCE) do not deviate significantly from the original AGV-1 starting material, $\delta^{56}Fe_{IRMM\text{-}14}$ and $\delta^{26}Mg_{DSM\text{-}3}$ range from −1.6‰ and −8.6‰, respectively, in the topmost portion (PCA) to 1.1‰ and 1.2‰ in the middle-third of the run product (PCC). Thus, the total offsets in $\delta^{56}Fe_{IRMM\text{-}14}$ and $\delta^{26}Mg_{DSM\text{-}3}$ are 2.8‰ and 9.8‰, respectively, much greater than the variation of Fe and Mg isotopes reported in terrestrial igneous samples (e.g., Beard and Johnson, 1999, 2004; Beard et al., 2003a, 2003b; Young and Galy, 2004; Poitrasson and Freydier, 2005; Weyer et al., 2005; Poitrasson, 2006; Schoenberg and Blanckenburg, 2006; Teng et al., 2007, 2008).

4.2. Results of STM-AGV-1

In contrast to the full-length thermal migration experiment which clearly brought part of the sample above liquidus temperatures, the STM-AGV-1 experiment, which started with the same wet andesitic powder, showed very few of the features documented above for LTM-AGV-1. The sample capsule was placed in a temperature gradient

Table 7
AMS data of experiment LTM-AGV-1.

K_m	K_1	K_2	K_3	L	F	P	P'	T	dK_1geo	iK_1geo	dK_2geo	iK_2geo	dK_3geo	iK_3geo
2.95E–05	3.24E–05	2.88E–05	2.72E–05	1.125	1.06	1.192	1.196	−0.34	355.5	83.3	262.9	0.3	172.8	6.7

The anisotropy of magnetic susceptibility (AMS) is usually approximated by a symmetric second rank tensor, which can be represented as an ellipsoid with three principal axes ($K_1 \geqslant K_2 \geqslant K_3$).
K_m: bulk magnetic susceptibility, measured at 300 A/m.
K_1: magnetic susceptibility along the longest axis of the AMS ellipsoid.
K_2: magnetic susceptibility along the intermediate axis of the AMS ellipsoid.
K_3: magnetic susceptibility along the shortest axis of the AMS ellipsoid.
The degree of anisotropy of the ellipsoid can be described by several parameters, e.g., the ratio P between the lengths of the maximum and minimum axes (Nagata, 1961) or the corrected anisotropy degree P'(Jelinek, 1981). $P' = \exp\sqrt{2\Sigma(lnK_i - K)^2}$ ($i = 1$–3, K is the arithmetic mean susceptibility). P' is a measure of the degree to which the AMS ellipsoid deviates from a sphere. In rocks having no preferred orientation of minerals the degree of anisotropy is equal to 1.
L, degree of linear anisotropy.
F, degree of planar anisotropy.
The shape of the AMS ellipsoid can vary from oblate, or disk-shaped, to prolate, or rod-shaped. $T = [(2\ln K_2 - \ln K_1 - \ln K_3)/(\ln K_1 - \ln K_3)]$. The magnetic ellipsoid is oblate (pancake shaped) for $0 \leqslant T_j \leqslant 1$ and prolate (pencil shaped) for $-1 \leqslant T_j \leqslant 0$.
dK_igeo and iK_igeo are declination and inclination of K_i ($i = 1$ to 3, K is the arithmetic mean susceptibility) in the geographic or sample framework, respectively.

Table 8
Variation of Mg–Fe isotope ratios of thermal migration samples with temperature in LTM-AGV-1.

	Position (mm)	$\delta^{56}Fe_{IRMM-14}$*	*n*	2SD	$\delta\ ^{26}Mg_{DSM-3}$@	*n*	2SD
PCA	17.5–18	−1.644	2	0.083	−8.34	3	0.60
PCB	12–15	−0.910	2	0.124	−6.50	2	0.46
PCC	9.2–11	1.120	3	0.009	1.53	2	0.22
PCD	3.2–6.2	0.080	2	0.017	−0.57	2	0.24
PCE	0–3.2	0.074	2	0.077	−0.60	2	0.14
ETH hematite	—	0.574	11	0.122	—	—	—
AGV-1	—	0.129	4	0.120	−0.12	5	0.25
RGM-1	—	0.186	1	—	—	—	—
BCR-2	—	−0.01	1	—	—	—	—

* All samples and standards were analyzed for Fe isotopes using both sample-standard bracketing and double-spike methods except RGM-1 and BCR-2 only by sample-standard bracketing.
@ Mg isotopes were measured using an in-house standard for bracketing.

for 33 days but with maximum temperature at the hot end of STM-AGV-1 of only ~550 °C. The run product does not contain visible glass, does not contain new crystals of hornblende, and does not display any compositional variation as a function of position. While BSE imaging of plagioclase grains does indicate some conversion to K-spar, no systematic enrichment of K_2O occurs at the cold of this experiment. The contrast between STM-AGV-1 and LTM-AGV-1 indicates that the melt plays a critical role in the differentiation of the partially molten andesite.

4.3. Simulations of LTM-AGV-1 using IRIDIUM

4.3.1. Simulations of major element behavior

IRIDIUM model simulations show good agreement with the mineralogical changes observed in the upper half of LTM-AGV-1. At the initiation ($t = 0$) of the simulation, the wet andesite starting material is predicted to be partially molten everywhere. However, after 50 days of simulation, the cold end (which is at 680 °C) evolves to become enriched in plagioclase and K-spar while the hot end becomes entirely molten. Indeed, the predicted sequence of melt → melt + mgt → melt + mgt + mafic → melt + mgt + mafic + plagioclase down temperature (Fig. 3F) closely follows that observed in the run product. The predicted Mg# of clinopyroxene decreases with temperature, consistent with the decrease in Mg# of amphibole observed in the experiment. Melt composition variation from IRIDIUM model is also generally consistent with experimental observation. In both IRIDIUM models and the LTM-AGV-1 experiment, melt compositions do not significantly change in the top all-melt portion but melt Mg# does decrease once amphibole appears. A key difference between simulation and experiment is that IRIDIUM fails to produce a cold end with a more silicic bulk composition or quartz saturation. This reflects the fact that IRIDIUM simulation must be run at >600 °C. Under these conditions, no quartz saturation occurs and thus there is no drive for silica to migrate to the cold end of the experimental capsule. However, quartz must be saturated at the temperatures of the cold end of LTM-AGV-1. The strong temperature dependence of quartz solubility in H_2O (Anderson and Burnham, 1965) provides a simple explanation for the observed deposition of quartz at the cold end.

Despite the fact that the simulation includes Soret coefficients to account for thermal diffusion, IRIDIUM predicts that the melt MgO content decreases down temperature, opposite to the prediction of a pure Soret simulation in which MgO is enriched at the cold end (Fig. 8D). This agrees with the observed melt compositional variation in the experiment and emphasizes that melt compositions during thermal migration are controlled by equilibration with coexisting mineral phases. In contrast, IRIDIUM simulations in a supra-liquidus temperature gradient reproduce trends observed in Soret experiments (e.g., MgO enrichment at the cold end). Thus, IRIDIUM demonstrates the major difference between the Soret effect (when only a single melt phase exists) and thermal migration: melt compositions during thermal migration are controlled by coexisting mineral phases and resemble liquid lines of descent and not trends of Soret separation (Fig. 8).

While IRIDIUM captures the general behavior of the experiment, several details are not reproduced, reflecting either the difficulty in modeling mineral saturation surfaces of complex minerals or the non-linear behavior of melt composition evolution which affects the details of saturation. For instance, amphibole-melt equilibrium is difficult to accurately model and this leads to clinopyroxene being the saturated mafic phase in the simulation. IRIDIUM also does not predict apatite as the liquidus phase as is observed. However, using the measured melt composition in the upper third of the experiment as input, the thermodynamic equilibrium program PELE (Boudreau, 1999) predicts apatite to be the liquidus phase. Thus, both IRIDIUM and PELE provide insight and reinforce general observations regarding the evolution of melt composition and mineral saturation with time during thermal migration.

4.3.2. Simulation of isotope fractionation by thermal diffusion

Significant Fe–Mg isotope fractionations are observed in the upper half of LTM-AGV-1. The observed fractionation does not appear to reflect equilibrium isotopic fractionation between phases or chemical diffusion but instead reflects thermal diffusion in a silicate melt (see below for more discussion). Because IRIDIUM includes the ability

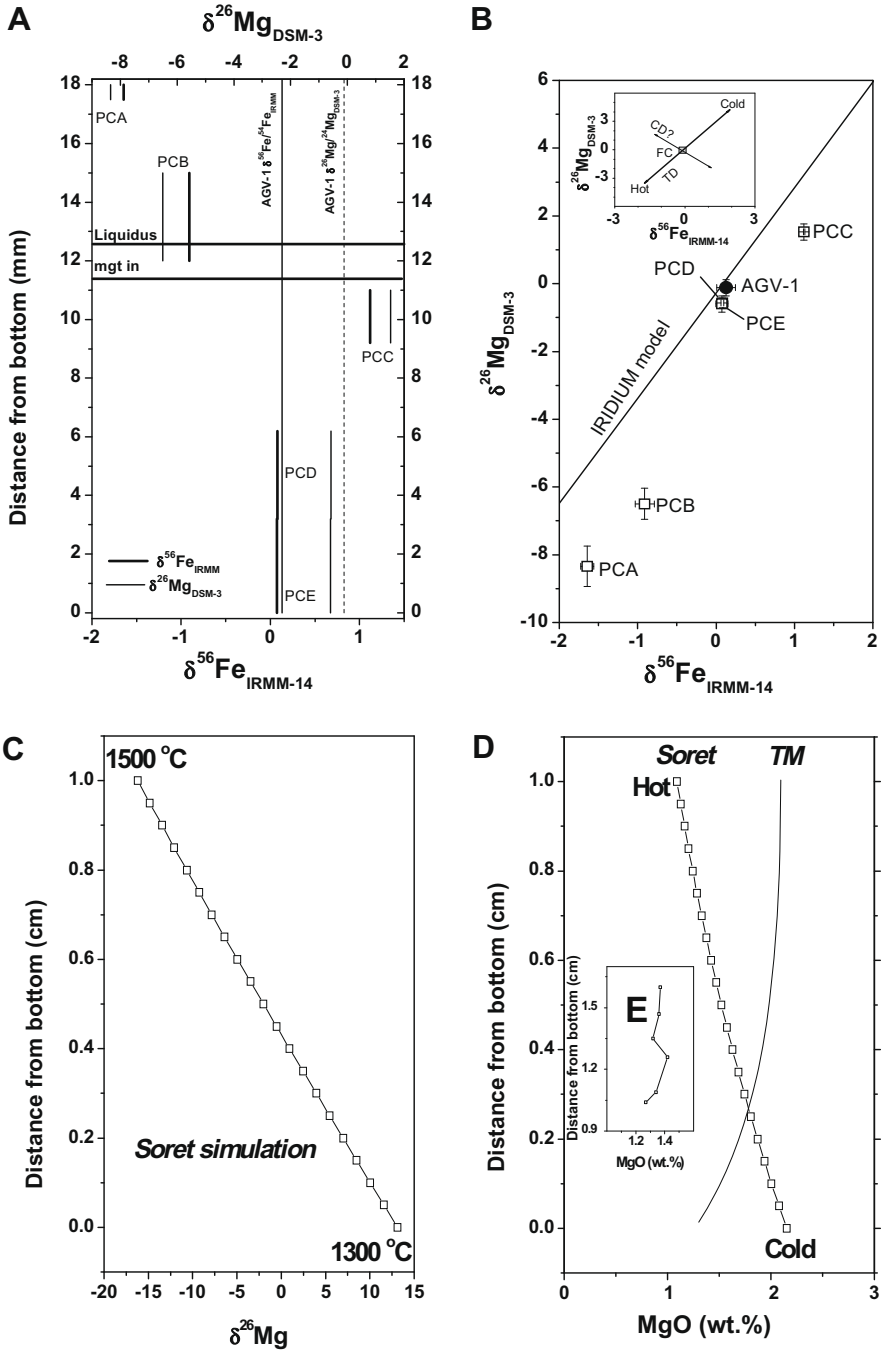

Fig. 8. (A) Fe–Mg isotope fractionation with distance from the base of the charge (LTM-AGV-1). Fe and Mg isotopes are significantly fractionated in the top two thirds of the charge while the bottom crystalline portion is isotopically similar to the starting materials. (B) Fe and Mg isotopic fractionation are linearly correlated with the lighter isotopes being enriched at the hottest end of the experiment, consistent with the simulation by the IRIDIUM models. The inserted panel shows predicted co-variation of Fe and Mg isotope ratios by fractional crystallization (FC), chemical diffusion (CD), and thermal diffusion (TD): FC results in limited isotopic variation (Teng et al., 2007); assuming opposite directions of Fe and Mg chemical diffusion would lead to negative CD correlation; TD always produces a positive correlation between Fe and Mg isotope ratios. Error bars reflect 2 SD for 2–5 analyses. C–D: IRIDIUM simulation for variations of δ^{26}Mg and MgO content of melt predicted for Soret and thermal migration (TM) processes. (C) Assuming that the heavy Mg isotope has greater D_T (Richter et al., 2008), the IRIDIUM simulation can produce Mg isotope variation with the cold end enriched in heavy isotopes. (D) MgO content increases with the decrease of temperature in the Soret simulation, while the MgO content of melt in the thermal migration simulation decreases with temperature because of equilibrium with coexisting mafic minerals (i.e., cpx). This is generally consistent with the variation of MgO with position in LTM-AGV-1 experiment (inset E).

to simulate thermal diffusion, we have used it to investigate isotopic effects in a silicate melt. IRIDIUM calculates the thermal diffusion flux through addition of term to the advection diffusion equation. This term combines the Soret coefficient and temperature gradient between nodes to drive element migration in the melt. While better constraint on Soret coefficients and chemical diffusion coefficients would be desirable, the present IRIDIUM modeling provides useful insight into investigating isotope fractionation by thermal diffusion and its interplay with chemical diffusion.

In order to determine isotopic variations using IRIDIUM, we first ran a simulation using a set of values for the chemical and thermal diffusion coefficients for each element. We then ran a second simulation changing these coefficients slightly to reflect the different diffusivity of an isotope of the same element. The outputs from the two runs were then combined to evaluate the predicted change in isotope ratios with position. Fig. 8b shows results for an andesite bulk composition Soret simulation using a 20-node distribution over 2 cm with temperature varying linearly from 1500 to 1300 °C. We assumed chemical diffusivities of 5×10^{-6} cm^2/s for all oxides and used Soret coefficients (denoted as σ) for Mount Hood Andesite from Lesher and Walker (1991) such that D_T for each element was prescribed based on $\sigma = D_T/D_C$. We assume that the mass dependence of chemical diffusion coefficients (D_C) and thermal diffusion coefficients (D_T) of Fe or Mg isotopes can be expressed as: $\frac{D_C^{56Fe}}{D_C^{54Fe}} = \left(\frac{54}{56}\right)^{\beta_C^{Fe}}$ and $\frac{D_C^{26Mg}}{D_C^{24Mg}} = \left(\frac{24}{26}\right)^{\beta_C^{Mg}}$; $\frac{D_T^{56Fe}}{D_T^{54Fe}} = \left(\frac{56}{54}\right)^{\beta_T^{Fe}}$ and $\frac{D_T^{26Mg}}{D_T^{24Mg}} = \left(\frac{26}{24}\right)^{\beta_T^{Mg}}$, where β_C and β_T are the parameters for the mass dependence of D_C and D_T, respectively.

The IRIDIUM simulations of the Soret process produce heavy isotope enrichment in the cold end of the simulation with a positive linear correlation between Mg and Fe isotope ratios (Fig. 8B). The slope of the trend depends on β_C and β_T for both Mg and Fe, some of which are poorly constrained. The values for the β_C for Mg and Fe are set as 0.05 while β_T^{Mg} is set at 0.5 (Richter et al., 2003, 2008). No experimental constraint on β_T^{Fe} currently exists. Simulation by IRIDIUM models using β_T^{Fe} of 0.45 produces a slope for $\delta^{26}Mg_{DSM\text{-}3}$ vs. $\delta^{56}Fe_{IRMM\text{-}14}$ of ~3.1, similar to that observed in our experiment. For this simulation of 200 °C offset, the total offsets for $\delta^{56}Fe_{IRMM\text{-}14}$ and $\delta^{26}Mg_{DSM\text{-}3}$ are 9.4 and 29.3‰, respectively. Accounting for differences in ΔT, these are ~1.5× greater than observed in experiments in either this study or Richter et al. (2008). Despite this difference, the simulations usefully show that the Soret coefficient for a heavy isotope is always more positive than that of a light isotope, regardless of the sign of the component's Soret coefficient. This is consistent with the result of a study of Soret effects in benzene–cyclohexane mixtures. In that study, the sign of the Soret coefficient was a function of chemical composition of the mixture, but heavy isotope enriched benzene always had a more positive Soret coefficient than light isotope enriched benzene (Debuschewitz and Köhler, 2001).

Thus, in the simple case of a single phase, IRIDIUM can be used to assess experimental results and illustrates the dominance of thermal diffusion over chemical diffusion in producing isotopic fractionation. Unfortunately, using IRIDIUM to assess isotopic fractionation during thermal migration simulations does not work because the sharp changes in concentrations in the melt dictated by phase saturation lead to erratic swings in predicted isotope fractionation with position.

5. DISCUSSION

5.1. Assessment of mass balance, local equilibrium and comparison with previous thermal migration experiments

The distribution of major elements and water in LTM-AGV-1 is consistent with full mass balance and closed system behavior during the experiment (Table 4). For water, in particular, this observation is notable because of the long duration of the experiment. Further, energy dispersive analysis of the Au-Pd capsule indicated no resolvable Fe content, confirming that there was no Fe loss due to alloying with the capsule. Mass-balance assessments of almost all trace-elements are also consistent with expected concentrations. Exceptions to this are Rb, Ba, and Li, elements that are often contaminated by inputs from noble metal capsules. Nevertheless, even though contaminant input occurred for these elements, the long duration of the experiment and the evidence that other trace-elements followed equilibrium partitioning argues that even Rb, Ba, and Li were distributed according to their phase partitioning behavior.

A partially molten silicate in a temperature gradient should evolve to become fully molten at the hot end and a fully compacted melt-free crystalline material at the cold end (Walker et al., 1988). The LTM-AGV-1 experiment did not reach this condition and if left to run longer, final compositional variations would differ somewhat from those that we observed. Nevertheless, this 66 day constant pressure/temperature gradient experiment represents one of the longest water bearing piston cylinder experiments yet performed. Several pieces of evidence suggest that LTM-AGV-1 closely approached local equilibrium between melt and crystals. First, values for the Mg–Fe exchange coefficient between amphibole and melt ($^{melt\text{-}amph}K_{Fe\text{–}Mg}$) are ~0.55, close to observed values in previous amphibole-melt experiments (Adam and Green, 1994; Brenan et al., 1995; Tiepolo et al., 2000). Second, in situ measured values of $^{plg/melt}D_{Sr}$ compare well with laboratory partitioning experiments (Bindeman and Davis, 2000), indicating a close approach to plagioclase-melt equilibrium. Third, there is a good general correspondence between trace-element content variations and element partitioning based on observed modes of mineral phases. Finally, there is good agreement between the trends in mineralogical change predicted by IRIDIUM and those observed in the experiment.

While previous thermal migration experiments did not use as large a temperature offset as that used here and investigated more mafic compositions under dry conditions, similarities between these studies and our results argue for common processes occurring during thermal migration, regardless of composition. For instance, the MORB composition experiments of Lesher and Walker (1988) also evolved to a completely molten hot end and crystal-rich

cold end, with the crystal-rich mat growing at 3.8 cm/yr. In comparison, using the disappearance of quenched glass at 8.5 mm, the LTM-AGV-1 indicates an average growth rate of the crystal-rich mat of 4.7 cm/yr. Similarly, both LTM-AGV-1 and previous experiments show melt MgO contents decreasing (and K_2O contents increasing) down temperature gradient, opposite to the trends of these elements predicted by Soret effects. Finally, plagioclase An content in both studies decreases down temperature initially and then progressively increases to higher An content toward the cold end.

5.2. Features of thermal migration behavior

We emphasize three important observations from the LTM-AGV-1 experiment: (1) a wet, partially molten silicate material in a temperature gradient self-differentiates into a granitic composition material at temperatures less than 400 °C; (2) large co-variations in Mg and Fe isotope ratios occur and are recorded in minerals as well as melt reflecting thermal diffusion in the upper half of the experiment; (3) a significant mineral fabric develops in the experiment. Below, we discuss issues in the development of these features, followed by implications for Earth processes.

Neither convection nor gravitational settling plays an important role in the mineralogical or compositional change in the experiment; instead, like previous thermal migration studies, chemical transport occurs by diffusion. The major observation arguing against convection or mechanical separation of phases is the systematic change in isotope ratios of Fe and Mg in the upper half of the charge, the portion of the experiment most likely to support either of these processes. While in certain circumstances convection could produce stratification and preserve isotopic differences (Jellinek et al., 1999), the linearity of the δ^{56}Fe vs δ^{26}Mg and its consistency with production by thermal diffusion argue that the upper half of the experiment reflected diffusive and not convective processes. Further evidence comes from trace-element and major element analysis of the melt in the top portion which shows no evidence for lateral heterogeneity as would occur if convection occurred. While a calculated Rayleigh number of 61 indicates convection could occur, the high aspect ratio cylindrical charge would likely inhibit convection because the interaction of the capsule walls with the high viscosity melt, unaccounted for in the Rayleigh number calculated, would be significant.

Similarly, gravitational settling does not provide a consistent explanation for several observations including the isotopic results. First, a simple Stroke's law calculation suggests that magnetite ($\rho = 5$ g/cm^3; grain size $= 50$ μm) would settle < 0.8 mm in a hydrous andesitic melt ($\sim$2.5 g/cm^3) with viscosity of $\sim 10^5$ PaS (Richet et al., 1996), much shorter than the actual length from the top of the capsule. Moreover, although mineral precipitation times could differ, the mineral sequence observed is not consistent with the order of settling predicted by mineral density. For instance, the magnetite layer occurs below apatite, but above amphibole and plagioclase. In contrast, the mineral layering follows the predicted order of saturation and thus is consistent with previous observations from temperature gradient based experiments (Lesher and Walker, 1988; Lundstrom et al., 2005). Perhaps most convincing, it is difficult to see how the linear co-variation of Fe and Mg isotopes could be produced by amphibole and magnetite crystallization and settling, particularly since the two overlying isotopic samples reflect the all-glass portion of the experiment. Indeed, the linear isotopic variation is well explained by thermal diffusion, given the similarities to other recent experiments (Richter et al., 2008).

Another important interpretation is that the melt in the top half of the experiment was under-saturated in H_2O. The lack of bubbles supports this interpretation, although the long time scale of the experiment could lead to separation of a vapor phase if it existed. A stronger argument comes from examining the H_2O content of the glass; the $\sim$7 wt.% that we measured is a value consistent with mass balance based on H_2O initially added. Such a concentration is below the known water saturation concentration for intermediate composition silicate melts at this pressure. For instance, regression of the H_2O concentration data from water-saturated experiments of Moore and Carmichael (1998) indicate that at 5 kbars, water saturation should occur $\sim$8.5 wt.% H_2O for an andesitic melt. Based on the lower water contents measured here and lack of any evidence for water saturation, we conclude that the melt at the top of the experiment was water-under-saturated.

5.2.1. *Differentiation at <500 °C by wet thermal migration*

Chemical differentiation occurs everywhere in LTM-AGV-1, including the bottom portion at <500 °C. This is clearly indicated by changes in both major- and trace-element compositions in the lower half of the charge relative to the starting material. This is also indicated by the growth of potassium feldspar and significant enrichment in bulk K_2O and SiO_2 content at the capsule bottom, and by significant changes from initial composition for almost every major element. These compositional changes require that some mechanism of fast chemical transport exist in the lower half of the charge. The low temperature based on our inferred temperature profile is corroborated by the presence of $\sim Or_{90}$ K-spar and fluorite in the bottom part of the experiment.

While we know that differentiation and thus chemical transport occurred within the lower half of the experiment, the process by which transport happened is somewhat enigmatic, given the very low temperatures at this end. While there may be other possibilities, we simplify this issue by considering several end-member processes: (1) chemical transport occurs by dry grain-boundary diffusion and involves dry sintering of subsolidus andesite starting material; or (2) transport occurs through a cryptic fluid or melt phase; or (3) transport occurs solely through solid lattice diffusion. Because lattice diffusion coefficients are known to be extremely small, mechanism #3 can be discarded. In contrast, much less is known about the diffusivity of elements during dry grain-boundary diffusion but it is likely to be significantly lower than for diffusion through either a melt or hydrous fluid. For instance, grain-boundary diffusion coefficients for the driest experiments of Yund

(1997) are much closer in magnitude to lattice diffusion coefficient rather than melt diffusion coefficients. A minimum effective diffusion coefficient for silica transport (D_{SiO2}) over the 1.8 cm length of the charge in 66 days (assuming $l=(Dt)^{0.5}$) is $\sim 6 \times 10^{-7}$ cm^2/s. Such a value is remarkably high for a fluid at <500 °C, let alone dry grain-boundary diffusion. Thus, while sintering can account for recrystallization and grain growth at subsolidus temperatures, in order for this mechanism to explain the observations, significant transport must occur by dry grain-boundary diffusion and it is not clear that this is possible. The clear growth of accessory phases such as zircon in the lower half would require transport of high field strength elements with likely low diffusivity, such as Zr. Finally, the lack of similar behavior in STM-AGV-1 where the entire experiment remained subsolidus appears to point toward an important role for melt in the overall process.

Given the rapid transport needed, we conclude that some type of fluid existed in the lower half of the charge. However, no visual evidence for a fluid exists other than a small amount of porosity, which could have been produced during sample preparation. Further, no sharp bubble-like interfaces, like those that develop between immiscible liquids, occur anywhere in the run product. This raises two important questions about the fluid present in the cold end of the charge: why does it exist and what is its composition?

There are three possibilities for explaining the inferred fluid at the cold end of LTM-AGV-1: (1) it could reflect hydrous melt only; (2) it could reflect hydrous fluid only; (3) it could reflect coexisting hydrous fluid and melt. While the <500 °C temperatures appear to argue against #1, we conclude that only a single melt phase existed and it was present throughout the charge. This is the most consistent with the experimental observations, with known phase equilibria (Tuttle and Bowen, 1958), and with observations from inclusions in natural magmatic materials (Sirbescu and Nabelek, 2002). The possibilities #2 and #3 can be eliminated because no separate hydrous fluid should exist in the experiment because the melt in the hot end of LTM-AGV-1 is water under-saturated. Furthermore, if water saturation did exist, experiments in simple systems indicate that hydrous fluid and silicate melt are immiscible at the pressure of this experiment. For instance, albitic melt and H_2O are miscible only at $\geqslant$15 kbars (Shen and Keppler, 1997) and the critical endpoint in the silica-H_2O system occurs at ~10 kbars (Kennedy et al., 1962). Therefore, we conclude that a separate supercritical hydrous fluid phase did not exist anywhere in this experiment.

Understanding why a melt would exist at temperatures thought to be subsolidus comes from examination of the classic work by Tuttle and Bowen (1958). Phase equilibrium experiments in the K_2O–Al_2O_3–SiO_2–H_2O system show that, as the melt composition becomes rich in K_2SiO_3 component relative to Al_2O_3, a hydrous melt still coexists with quartz and orthoclase at < 400 °C (Na_2SiO_3 has the same effect; Tuttle and Bowen, 1958). Tuttle and Bowen (1958) explicitly state that the presence of alkali silicate components beyond the amount combining with alumina to make alkali feldspar leads to major depression of the solidus temperature, providing for a continuum of melt compositions down to hydrothermal-like fluids coexisting with quartz and alkali feldspar.

While Tuttle and Bowen (1958) argued that alkali silicate-rich fluid compositions were not relevant to silicic rock petrogenesis, they did not consider the role of a temperature gradient in producing such a liquid composition. The effect of a temperature gradient in the experiment is to drive potassium and silica toward the cold end of the gradient (where quartz and K-spar are saturated) and alumina toward hotter regions (where the peak in plagioclase mode occurs), resulting in a dynamic process that produces high K_2SiO_3/Al_2O_3 in the liquid at the cold end of the experiment. These predicted directions of K, Al, and Si migration are illustrated by the compositional changes observed in the LTM-AGV-1 experiment, in IRIDIUM models and in previous temperature gradient experiments (Lundstrom et al., 2005). Simply put, the reason for the chemical activity gradients and thus migration directions reflect phase saturation as a function of temperature. It is important to note that while the melt existing at these low temperatures may be peralkaline, the proportion of melt (based on the small porosity observed in the experiment) will be very small such that the bulk composition will not be greatly changed from that of the coexisting rock/minerals.

Evidence exists for low temperature, water-rich melts in granitic systems. Melt inclusions from the Tin Mountain pegmatite have microthermometry temperatures below 400 °C, reflecting the role of minor-element constituents (F, B) in lowering the solidus temperature (Sirbescu and Nabelek, 2002). The presence of fluorite in the cold end of LTM-AGV-1 suggests a similar role for F in reducing solidus temperatures. Similarly, the full miscibility observed during re-homogenization of melt inclusions in pegmatite quartz at 1 kbar and 700 °C indicates existence of a melt with ~22 wt% H_2O (Thomas et al., 2000). We thus suggest that the cold end melt in LTM-AGV-1 was very water-rich (30–50–wt.%?) with transport properties closer to supercritical H_2O than typical silicate melt. Further experiments on the critical behavior of multi-component silicates/H_2O at elevated pressure and temperature are needed to constrain possible melt compositions and properties (Manning and Schmidt, 2007).

Indeed, the inferred diffusivities from the experiment support the inference that the liquid resembled a supercritical H_2O in terms of transport properties. The $\sim 6 \times 10^{-7}$ cm^2/s diffusivity calculated above is generally consistent with previous work showing that D_{SiO2} in supercritical H_2O is very high (Idlefonse and Gabis, 1973; Watson and Wark, 1997). In detail, consideration of the liquid fraction present and tortuosity in the bottom portion of the experiment should result in much lower diffusivities than observed. This leads us to speculate that transport through the cold end involves continuous reaction and flow *through* crystals, as recently advocated by Oelker et al. (2007). These calculations indicate that igneous minerals in a temperature gradient can be extremely permeable to supercritical hydrous fluids because the rate of dissolution/precipitation of these minerals at moderately high-temperature (400 °C) is very rapid (Oelker et al., 2007).

In conclusion, the significant differentiation of wet andesite at subsolidus temperature leads us to infer the existence of a melt enriched in H_2O and alkali metasilicates at the cold end of LTM-AGV-1. While the differentiation of material at temperatures as low as 350 °C would appear to be outside of that considered "igneous," the process illustrated by LTM-AGV-1 is fully magmatic, occurring with a melt-present and with consistency to known mineral-melt phase equilibria. Indeed, the lack of differentiation occurring in the STM-AGV-1 experiment shows that both the high-temperature melt and coexisting mafic minerals are required to effectively differentiate material along the temperature gradient.

5.2.2. Fractionation of stable isotopes by thermal diffusion

A striking feature of LTM-AGV-1 is the occurrence of large variations in Fe and Mg isotope ratios in the upper half of the charge. Until recently, no known mechanisms could explain the observed variations. For instance, the equilibrium isotopic fractionation between minerals and melt at ~800 °C should be very small (e.g., Urey, 1947; Polyakov and Mineev, 2000; Polyakov et al., 2007) and other mechanisms such as chemical diffusion (Richter et al., 2003) or kinetic fractionation during redox reactions (Roskosz et al., 2006) appear unable to explain either the magnitude of isotopic fractionation or the co-variation in Mg and Fe isotope ratios. However, the close correspondence between our results and those in recent work by Richter et al. (2008) suggest that the large isotopic variations are produced by thermal diffusion.

Thermal diffusion has long been known to cause isotopic fractionation—lighter isotopes or species are always enriched at the hotter end of a temperature gradient (i.e., Furry et al., 1939; Ott, 1969; Reith and Muller-Plathe, 2000). However, only recently has thermal diffusion been shown to result in significant fractionation of isotopes in silicate melts (Kyser et al., 1998; Richter et al., 2008). LTM-AGV-1 shows the same hot end enrichment in light isotopes, with variations independent of the flux of these elements based on concentration changes.

Thermal diffusion sensitivity (Ω, defined as the isotopic fractionation with temperature variation with unit of ‰/°C/amu) is used to describe the magnitude of stable isotope fractionation along a temperature gradient (Severinghaus et al., 2001; Richter et al., 2008). The 126 °C temperature difference between PCC and PCA in LTM-AGV-1 indicates a Ω_{Mg} of ≈0.039‰/°C/amu. This compares well with the experiments of Richter et al. (2008): experiment SRT4 (100 h. duration) had Ω_{Mg} = 0.039‰/°C/amu while experiment SRT8 (64 h.) had Ω_{Mg} = 0.036‰/°C/amu. In contrast, Ω_{Fe} in LTM-AGV-1 is 0.011‰/°C/amu, considerably smaller than Ω_{Mg}. Recently, we analyzed Soret experiment ZM71 from Lesher and Walker (1986) and found total offsets of $\delta^{56}Fe_{IRMM\text{-}14}$ and $\delta^{26}Mg_{DSM3}$ of 6.1‰ and 16.7‰, respectively, producing Ω_{Fe} and Ω_{Mg} of 0.012‰/°C/amu and 0.032‰/°C/amu, consistent with the values observed in LTM-AGV-1 (Huang et al., 2008). Two first order conclusions can be made from the above observations: (1) the isotopic difference between the hot and cold end is proportional to the offset in temperature in a near steady-state, melt-present system; and (2) Mg shows greater sensitivity to temperature gradients than Fe.

Importantly, isotopic signatures of thermal diffusion in the melt are clearly recorded in coexisting minerals as shown by sample PCC (located mid-sample). The linearity of the $\delta^{56}Fe_{IRMM\text{-}14}$ vs $\delta^{26}Mg_{DSM\text{-}3}$ data, combined with the fact that most of the Mg and Fe atoms in sample PCC are bound in solid phases (amphibole and magnetite), argues that rocks formed by thermal migration will preserve an isotopic signature of thermal diffusion. However, the lower half of the experiment does not record any measurable change in $\delta^{56}Fe_{IRMM\text{-}14}$ and $\delta^{26}Mg_{DSM\text{-}3}$. This may reflect the reduced ability for isotopic exchange to occur at the bottom of the charge due to its high crystallinity or may reflect the fact that there is little if any mass dependence of thermal diffusion through the super-hydrous, Na_2O and K_2O rich melt at the bottom of the charge. Clearly, more work is needed to better understand the transport properties of such melt and to characterize the mass dependence of thermal diffusion for different elements in terms of melt structure and other parameters. An important point to reiterate is that while compositional trends of differentiation in a thermal gradient are controlled by mineral-melt equilibria and do not record concentration signatures of a Soret effect, the greater mass dependence of thermal diffusion relative to chemical diffusion will lead to production of isotopic signatures of diffusive differentiation in a thermal gradient.

5.2.3. Development of mineral fabric by thermal migration

Observations of elongate minerals and anisotropic magnetic fabric produced by growth in a temperature gradient add thermal migration as a possible mechanism influencing rock fabrics in the magmatic environment. The degree of anisotropy observed in the AMS measurement (1.2) is large and comparable in size to that observed in many magnetite bearing igneous rocks (granites: Ferré et al., 1999; layered mafic intrusions: Maes et al., 2007). The prolate symmetry of the magnetic fabric reflects the elongation of magnetite crystals grown in a temperature gradient.

Finding mineral elongation in temperature gradient experiments is not new. Walker et al. (1988) noted olivine elongation in their thermal migration experiments and similar textures of hornblende occur in LTM-AGV-1. However, the EBSD measurement in the lower half of the run product fails to find any preferred orientation of other minerals (plagioclase and biotite), indicating little ability for thermal migration to reorient minerals that formed at the onset of the experiment. This is consistent with our EBSD analyses of other thermal gradient experiments where only newly formed crystals showed preferred orientation (DeFrates et al., 2006).

5.3. Wet thermal migration as an igneous differentiation process

5.3.1. Possible role of thermal migration in differentiating magmas

The compositional changes in LTM-AGV-1 are large and occur due to wet thermal migration and not mechanical separation of crystals and melt. However, temperature gra-

dient driven mass transport processes have been largely considered unimportant to the Earth because temperature gradients around an emplaced magma are assumed to dissipate before significant mass diffusion occurs (because heat diffusion >> mass diffusion). However, this conclusion should be re-examined, given recent geochronological observations indicating that some intrusive rocks remain at elevated temperatures for million-year time scales. For instance, a well-studied pluton from the Sierra Nevada batholith has U–Pb zircon ages, which differ by 10 Myr between margin and core (Coleman et al., 2004), while Ar–Ar in hornblende and biotite dates are systematically younger than U–Pb ages (Kistler and Fleck, 1994). Prolonged time scales of cooling (and thus, elevated temperature) of possibly tens of millions of years appear to occur in other granitoid plutons and even silicic volcanic rocks (Bachmann and Bergantz, 2004; Siebel et al., 2005) while offsets in age based on different chronometers also occur in layered mafic intrusions (Hirschmann et al., 1997; Barfod et al., 2003). These observations rule out models whereby a single blob of magma is emplaced, cools and differentiates. Instead, silicic systems likely reflect sustained input of heat through magmatic underplating (Bergantz, 1989). Indeed, slow steady arrival of magma can lead to a moving steady-state temperature gradient zone, allowing wet thermal migration to be the major mechanism of differentiation in partially molten magmatic systems (Lundstrom et al., 2008).

One way of thinking about how thermal migration might differentiate magmas and affect trace-elements is by having interconnected melt in a mush zone in a temperature gradient. For instance, it is possible that trace-element signatures of amphibole fractionation observed in arc volcanic rocks (Davidson et al., 2007) reflect amphibole existing in a lower temperature mush and differentiating a hotter magma not saturated in amphibole by thermal migration. Similarly, clinopyroxene fractionation signatures could be imparted on MORB magmas interconnected with colder mush despite the paucity of clinopyroxene observed in MORB (Dungan and Rhodes, 1978).

5.3.2. Thermal migration: an explanation for $\delta^{56}Fe$ variations in igneous rocks?

Significant variations in non-traditional isotope systems (e.g., Fe, Mg) have now been observed in various igneous rocks and between minerals within a single rock. Although Fe isotopes show limited variation in mafic and intermediate igneous rocks (Beard and Johnson, 1999, 2004, 2006; Beard et al., 2003a), $\delta^{57}Fe_{IRMM\text{-}14}$ is up to 0.6‰ higher than typical mantle-derived rocks at higher silica contents ($SiO_2 > 71$ wt.%; Poitrasson and Freydier, 2005; Poitrasson, 2006). Per mil level variations in Fe isotopes have also been observed between phases in mantle xenolith samples (e.g., Williams et al., 2004, 2005). The reasons these variations occur in high-temperature samples remains widely debated (e.g., Beard and Johnson, 2006; Poitrasson, 2006).

Recent work suggests thermal diffusion provides a larger isotopic fractionation than chemical diffusion (Richter et al., 2008) or possibly equilibrium partitioning between phases. Thus, thermal diffusion could play an important role in causing stable isotope variations in igneous rocks if temperature gradients can persist for extended durations. The systematic increase in $\delta^{56}Fe$ in silicic igneous rocks may provide one example; observed variations in $\delta^{56}Fe$ and $\delta^{26}Mg$ in mantle xenoliths may provide a second example. Xenoliths, which can be envisioned as colder mantle lithospheric wall rocks along conduits for melt ascent, are likely to be susceptible to reactions occurring within a temperature gradient that could exist for millions of years (depending on how long the conduit exists). If so, variations in $\delta^{56}Fe$ and $\delta^{26}Mg$ between xenoliths and between minerals in single xenoliths may reflect records of thermal diffusion and thermal migration occurring on the edge of melt conduits.

The most important point to emphasize is that while major- and trace-element compositional signatures caused by thermal diffusion are not distinguishable from those of competing processes such as fractional crystallization or chemical diffusion, thermal diffusion will produce a unique isotopic signature. Isotopic measurements thus provide a tool for identifying thermal migration processes, if they occur in nature. Because thermal diffusion will always produce positive correlations between multiple stable isotope systems, signatures of thermal diffusion can be easily distinguished from other processes.

6. CONCLUSIONS

Partially molten wet andesite situated within an imposed temperature gradient (950–350 °C) undergoes dramatic changes in composition, mineralogy, isotopic composition and mineral fabric. Specifically:

1. A homogenous partially molten wet andesite differentiates into granitic bulk composition at the low temperature end of the gradient.
2. A hydrous melt exists at temperatures <400 °C, reflecting the role of a temperature gradient in forming melts with high alkali silicate to alumina ratios and leading to fast chemical transport through largely crystalline material.
3. Trace-element concentrations follow equilibrium partitioning into minerals distributed across the temperature gradient. Thus, trace-element contents in erupted lavas unsaturated in a given mineral may record signatures of that mineral's presence in a magma mush zone within a temperature gradient.
4. Thermal diffusion produces significant Fe and Mg isotope fractionations with the hotter region always enriched in lighter isotopes, providing a signature of the thermal migration process.
5. Significant anisotropy of magnetic susceptibility and hornblende alignment occur in a temperature gradient, in the absence of differential stress.
6. Mineralogical, compositional and isotopic variations during thermal migration can be reproduced using IRIDIUM models, providing a tool to examine the process at longer length scales.

In sum, wet thermal migration produces mineralogical, mineral fabric, and major and trace-element compositional

trends that resemble those in Earth's magmatic systems. Importantly, thermal migration also produces a unique fingerprint of the process, positive co-variation of stable isotopes. Future analyses of non-traditional stable isotopes thus provide the data to assess whether or not thermal migration might be a major process of igneous differentiation on Earth.

ACKNOWLEDGMENTS

We thank three anonymous reviewers and associate editor A. Brandon for their insightful comments which greatly helped to improve the manuscript. We thank A. Glazner, D. Henley, C. Miller, S. Kieffer, and T. Johnson who informally reviewed versions of the manuscript, Z. Zhang, C. Bopp, and K. Ireland for laboratory help, and C. Lesher and F.-Z. Teng for instructive discussion. We also thank Tim Spila for helping us with trace-element analyses in the Center for Microanalysis of Materials Frederick Seitz Materials Research Laboratory at UIUC. This work is supported by NSF EAR 0609726. Work in the MC-ICPMS lab is supported by NSF EAR 0732481.

APPENDIX A. SUPPLEMENTARY DATA

Supplementary data associated with this article can be found, in the online version, at doi:10.1016/j.gca.2008.11.012.

REFERENCES

Adam J. and Green T. H. (1994) The effects of pressure and temperature on the partitioning of Ti, Sr and REE between amphibole, clinopyroxene and basanitic melts. *Chem. Geol.* **117**, 219–233.

Anderson G. M. and Burnham C. W. (1965) The solubility of quartz in supercritical water. *Am. J. Sci.* **263**, 494–511.

Bachmann O. and Bergantz G. W. (2004) On the origin of crystal-poor rhyolites: extracted from batholithic crystal Mushes. *J. Petrol.* **45**, 1565–1582.

Barfod G. H., Otero O. and Albarède F. (2003) Phosphate Lu–Hf geochronology. *Chem. Geol.*, 241–253.

Beard B. L. and Johnson C. M. (1999) High precision iron isotope measurements of terrestrial and lunar materials. *Geochim. Cosmochimica Acta* **63**, 1653–1660.

Beard B. L. and Johnson C. M. (2004) Inter-mineral Fe isotope variations in mantle-derived rocks and implications for the Fe geochemical cycle. *Geochemistry Geophysics Geosystems* **68**, 4727–4743.

Beard B. L. and Johnson C. M. (2006) Comment on "Heavy iron isotope composition of granites determined by high resolution MC-ICP-MS", by F. *Poitrasson and R. Freydier. Chemical Geology* **235**, 201–204.

Beard B. L., Johnson C. M., Damm K. L. V. and Poulson R. L. (2003a) Iron isotope constrains on Fe cycling and mass balance in oxygenated Earth oceans. *Geology* **31**, 629–632.

Beard B. L., Johnson C. M., Skulan J. L., Nealson K. H., Cox L. and Sun H. (2003b) Application of Fe isotopes to tracing the geochemical and biological cycling of Fe. *Chemical Geology* **195**, 87–117.

Bergantz G. W. (1989) Underplating and Partial Melting: Implications for Melt Generation and Extraction. *Science* **245**, 1093–1096.

Bindeman I., Davis A. and Drake M. (1998) Ion microprobe study of plagioclase-basalt partition coefficients at natural concentration levels of trace elements. *Geochim. Cosmochem. Acta* **62**, 1175–1193.

Bindeman I. N. and Davis A. M. (2000) Trace element partitioning between plagioclase and melt: investigation of dopant influence on partition behavior. *Geochim. Cosmochim. Acta* **64**, 2863–2878.

Boudreau A. E. (1999) PELE—a version of the MELTS software program for the PC platform. *Comput. Geosci.* **25**, 201–203.

Boudreau A. E. (2003) IRIDIUM—a program to model reaction of silicate liquid infiltrating a porous solid assemblage. *Comput. Geosci.* **29**, 423–429.

Bowen N. L. (1915) Crystallization–differentiation in silicate liquids. *Am. J. Sci.* **39**, 175–191.

Brady J. B. (1995) Diffusion data for silicate minerals, glasses, and liquids. *Mineral Physics and Crystallography A Handbook of Physical Constant*, vol. 111, pp. 269–290.

Brenan J. M., Shaw H. F., Ryerson F. J. and Phinney D. L. (1995) Experimental determination of trace-element partitioning between pargasite and a synthetic hydrous andesitic melt. *Earth Planet. Sci. Lett.* **135**, 1–11.

Buchwald V. F., Kjer T. and Tborsen K. A. (1985) Thermal migration I: or how to transport iron sulfide in solid iron meteorites. *Meteoritics* **20**, 617–618.

Coleman D. S., Gray W. and Glazner A. F. (2004) Rethinking the emplacement and evolution of zoned plutons: geochronologic evidence for incremental assembly of the Tuolumne Intrusive Suite, California. *Geology* **32**, 433–436.

Davidson J., Turner S., Handley H., Macpherson C. and Dosseto A. (2007) Amphibole "sponge" in arc crust? *Geology* **35**, 780–787.

Debuschewitz C. and Köhler W. (2001) Molecular origin of thermal diffusion in benzene l cyclohexane mixtures. *Phys. Rev. Lett.* **87**. doi:10.1103/PhysRevLett.87.055901.

DeFrates, J., Lundstrom, C.C. and Marshak, S. (2006). Can diffusion in a thermal gradient produce crystallographic preferred orientation? GSA *Annual Meeting, Philadelphia*, (Abstr. 170-15).

Ding X., Sun W. D., Huang F., Lundstrom C. C. and Li J. (2007) Different mobility of Nb and Ta along a thermal gradient. *Geochim. Cosmochimica Acta*. Goldschmidt abstracts.

Dungan M. A. and Rhodes J. M. (1978) Residual glasses and melt inclusions in basalts from DSDP Legs 45 and 46: evidence for magma mixing. *Contrib. Mineral. Petrol.* **67**, 417–431.

Ferré E. C., Wilson J. and Gleizes G. (1999) Magnetic susceptibility and AMS of the Bushveld alkaline granites, South Africa. *Tectonophysics* **307**, 113–133.

Flanauan F. (1967) U.S. Geological Survey silicate rock standards. *Geochim. Cosmochim. Acta* **31**, 289–308.

Furry W. H., Jones R. C. and Onsager L. (1939) On the theory of isotope separation by thermal diffusion. *Phys. Rev.* **55**, 1083–1095.

Hauri E., Wang J., Dixon J. E., King P. L., Mandeville C. and Newman S. (2002) SIMS analysis of volatiles in silicate glasses: 1. Calibration, matrix effects and comparisons with FTIR. *Chem. Geol.* **183**, 99–114.

Hirschmann M. M., Renne P. and McBirney A. R. (1997) $^{40}Ar/^{39}Ar$ dating of the Skaergaard intrusion. *Earth Planet. Sci. Lett.* **146**, 645–658.

Huang F., Lundstrom C. C. and Lesher C. E. (2008) Fe–Mg isotope fractionation in silicate melt by thermal diffusion. *Goldschmidt Conference abstract*.

Idlefonse J.-P. and Gabis V. (1973) Experimental study of silica diffusion during metasomatic reactions in the presence of water

at 550 C and 1000 bars. *Geochim. Cosmochim. Acta* **40**, 297–303.

Jelinek V. (1981) Characterisation of the magnetic fabrics of rocks. *Tectonophysics* **79**, 63–67.

Jellinek A. M., Kerr R. C. and Griffiths R. W. (1999) Mixing and compositional stratification produced by natural convection 1. Experiments and their application to Earth's core and mantle. *J. Geophys. Res.* **104**, 7183–7201.

Kennedy G. C., Wasserburg G. J., Heard H. C. and Newton R. C. (1962) The upper three-phase region in the system SiO_2–H_2O. *Am. J. Sci.* **260**, 501–521.

Kistler R. and Fleck R. (1994) Field guide for a transect of the central Sierra Nevada, California; geochronology and isotope geology. Open-File Report—U. S. Geological Survey, Report: OF 94-0267, p. 50

Kushiro I. (1990). *J. Geophys. Res.* **95**, 15929–15939.

Kyser T. K., Lesher C. E. and Walker D. (1998) The effects of liquid immiscibility and thermal diffusion on oxygen isotopes in silicate liquids. *Contrib. Mineral. Petrol.* **133**, 373–381.

Lesher C. E. and Walker D. (1986) Solution properties of silicate liquids from thermal diffusion experiments. *Geochim. Cosmochim. Acta* **50**, 1397–1411.

Lesher C. E. and Walker D. (1988) Cumulate maturation and melt migration in a temperature-gradient. *J. Geophys. Res.* **B9**, 10295–10311.

Lesher C. E. and Walker D. (1991). Thermal diffusion in petrology. In *Diffusion, Atomic Ordering, and Mass Transport* (ed. J. Ganguly). *Advances in Physical Geochemistry*, vol. 8. Springer-Verlag, New York, pp. 396–451.

Lundstrom C., Boudreau A. and Pertermann M. (2005) Diffusion-reaction in a thermal gradient: implications for the genesis of anorthitic plagioclase, high alumina basalt and igneous mineral layering. *Earth Planet. Sci. Lett.* **237**, 829–854.

Lundstrom C. C., Huang F. and Glessner J. (2008) Temperature gradient driven magma differentiation and isotopic fractionation. *Goldschmidt Conference abstract*.

Maes S. M., Tikoff B., Ferré E. C., Brown P. E. and Miller J. (2007) Internal structure and emplacement history of the Sonju Lake Intrusion, northeast Minnesota inferred from magnetic fabrics. *Precambrian Res.* **157**, 269–288.

Manning C. E. and Schmidt C. (2007) Changes in ion pairing across the H_2O liquid–liquid transition: implications for planetary fluids. *GCA Goldschmidt abstracts*.

Morse S. A. (1992) Partitioning of strontium between plagioclase and melt: a comment. *Geochim. Cosmochim. Acta* **56**, 1735–1737.

Moore G. M. and Carmichael I. S. E. (1998) The hydrous phase equilibria (to 3 kbar) of an andesite and basaltic andesite from Western Mexico: constraints on water content and conditions of phenocryst growth. *Contributions to Mineralogy and Petrology* **130**, 304–319.

Nagata T. (1961) Rock Magnetism. Maruzen Ltd., Tokyo, Chapters 1–3, p. 350.

Oelker E. H., Putnis C. V. and Putnis A. (2007) Do fluids flow through or around mineral grains? *Geochim. Cosmochim. Acta* **71**, A729.

Ott A. (1969) Isotope separation by thermal diffusion in liquid metal. *Science* **164**, 297.

Pertermann M. and Lundstrom C. C. (2006) Phase equilibrium experiments at 0.5 GPa and 1100–1300 C on a basaltic andesite from Arenal volcano, Costa Rica. *J. Volcanol. Geothermal Res.* **157**, 222–235.

Pickering J. M., Schwab B. E. and Johnson A. D. (1998) Off-center hot spots: double thermocouple determination of the thermal gradient in a 1.27 cm (1/2 in.) CaF2 piston–cylinder furnace assembly. *Am. Mineral.* **83**, 228–235.

Poitrasson F. (2006) On the iron isotope homogeneity level of the continental crust. *Chem. Geol.* **235**, 195–200.

Poitrasson F. and Freydier R. (2005) Heavy iron isotope composition of granites determined by high resolution MC-ICP-MS. *Chem. Geol.* **222**, 132–147.

Polyakov V. B., Clayton R. N., Horita J. and Mineev S. D. (2007) Equilibrium iron isotope fractionation factors of minerals: reevaluation from the data of nuclear inelastic resonant X-ray scattering and Mossbauer spectroscopy. *Geochim. Cosmochim. Acta* **71**, 3833–3846.

Polyakov V. B. and Mineev S. D. (2000) The use of Mössbauer spectroscopy in stable isotope geochemistry. *Geochem. Geophys. Geosyst.* **64**, 849–865.

Reith D. and Muller-Plathe F. (2000) On the nature of thermal diffusion in binary Lennard–Jones liquids. *J. Chem. Phys.* **112**, 2436–2443.

Richet P., Lejeune A.-M., Holtz F. and Roux J. (1996) Water and the viscosity of andesite melts. *Chemical Geology* **128**, 185–198.

Richter F. M., Davis A. M., DePaolo D. J. and Watson E. B. (2003) Isotope fractionation by chemical diffusion between molten basalt and rhyolite. *Geochim. Cosmochim. Acta* **67**, 3905–3923.

Richter F. M., Watson E. B., Mendybaev R., Teng F.-Z. and Janney P. (2008) Magnesium isotope fractionation in silicate melts by chemical and thermal diffusion. *Geochim. Cosmochim. Acta* **72**, 206–220.

Roskosz M., Luais B., Watson H. C., Toplis M. J., Alexander C. M. O. D. and Mysen B. O. (2006) Experimental quantification of the fractionation of Fe isotopes during metal segregation from a silicate melt. *Earth Planet. Sci. Lett.* **248**, 851–867.

Schoenberg R. and Blanckenburg F. v. (2006) Modes of planetary-scale Fe isotope fractionation. *Earth Planet. Sci. Lett.* **252**, 342–359.

Severinghaus J. P., Grachev A. and Battle M. (2001) Thermal fractionation of air in polar firn by seasonal temperature gradients. *Geochim. Geophys, Geosys.* **2,** #2000GC000146.

Shen A. and Keppler H. (1997) Direct observation of complete miscibility in the albite-H_2O system. *Nature* **385**, 710–712.

Siebel W., Reitter E., Wenzel R. and Blaha U. (2005) Sr isotope systematics of K-feldspars in plutonic rocks revealed by the Rb–Sr microdrilling technique. *Chem. Geol.* **222**, 183–199.

Sirbescu M.-L. C. and Nabelek P. I. (2002) Crustal melts below 400 C. *Geology* **31**, 685–688.

Teng F.-Z., Wadhwa M. and Helz R. T. (2007) Investigation of magnesium isotope fractionation during basalt differentiation: implications for a chondritic composition of the terrestrial mantle. *Earth Planet. Sci. Lett.* **261**, 84–92.

Teng F.-Z., Dauphas N. and Helz R. T. (2008) Iron isotope fractionation during magmatic differentiation in Kilauea Iki lava lake. *Science* **320**, 1620–1622.

Thomas R., Webster J. D. and Heinrich W. (2000) Melt inclusions in pegmatite quartz: complete miscibility between silicate melts and hydrous fluids at low pressure. *Contrib. Mineral. Petrol.* **139**, 394–401.

Tiepolo M., Vannucci R., Oberti R., Foley S., Bottazzi P. and Zanetti A. (2000) Nb and Ta incorporation and fractionation in titanian pargasite and kaersutite: crystal-chemical constraints and implications for natural systems. *Earth Planet. Sci. Lett.* **176**, 185–201.

Tuttle, O.F. and Bowen, N.L. (1958). Origin of granite in the light of experimental studies in the system $NaAlSi_3$ O_8 $KAlSi_3O_8$—SiO_2—H_2 O. *Geol. Soc. America Mem.* 74.

Urey H. C. (1947) The thermodynamics of isotopic substances. *J. Chem. Soc. Lond.* **1947**, 562–581.

Walker D. and DeLong S. E. (1982) Soret separation of mid-ocean ridge basalt magma. *Contrib. Mineral. Petrol.* **79**, 231–240.

Walker D., Jurewicz S. and Watson E. B. (1988) Adcumulus dunite growth in a laboratory thermal gradient. *Contrib. Mineral. Petrol.* **99**, 306–319.

Walker D., Lesher C. E. and HAYS J. F. (1981) Soret separation of lunar liquid. In *Proc. Lunar Planet. Sci. Conf. 12th*. pp. 991–999.

Watson E. B. and Wark D. A. (1997) Diffusion of dissolved SiO_2 in H_2O at 1 GPa, with implications for mass transport in the crust and upper mantle. *Contrib. Mineral. Petrol.* **130**, 66–80.

Weyer S., Anbar A. D., Brey G. P., Münker C., Mezger K. and Woodland A. B. (2005) Iron isotope fractionation during planetary differentiation. *Earth Planet. Sci. Lett.* **240**, 251–264.

Williams H. M., McCammon C. A., Peslier A. H., Halliday A. N., Teutsch N., Levasseur S. and Burg J.-P. (2004) Iron isotope fractionation and the oxygen fugacity of the mantle. *Science* **304**, 1656–1659.

Williams H. M., Peslier A. H., McCammon C., Halliday A. N., Levasseur S., Teutsch N. and Burg J.-P. (2005) Systematic iron isotope variations in mantle rocks and minerals: the effects of partial melting and oxygen fugacity. *Earth Planet. Sci. Lett.* **235**, 435–452.

Young E. D. and Galy A. (2004) The isotope geochemistry and cosmochemistry of magnesium. In *Geochemistry of Non-Traditional Stable Isotopes, Reviews in Mineralogy and Geochemistry*, vol. 55 (eds. C. M. Johnson, B. L. Beard and F. Albarede). Mineralogical Society of America, Washington, pp. 197–230.

Yund R. (1997) Rates of grain boundary diffusion through enstatite and forsterite reaction rims. *Contrib. Mineral. Petrol.* **126**, 224–236.

Associate editor: Alan D. Brandon